

3

Tyres

3.1 Background

Road–tyre interactions have been modelled classically using two nonholonomic constraints (such as those discussed in Sections 2.9 and 2.10), which is a reasonable approximation at very low speeds. At the end of the nineteenth century this model came into question when it was recognized (using tests with rubber models) that there were distinct adhesion and sliding regions in the tyre’s contact patch. This discovery led to the concept of (longitudinal) ‘tyre slip’ [80]. The same ideas were later applied to lateral slip, which was recognized as being responsible for the directional stability of guided wheels and ‘shimmy’ [81].¹ It was again shown by measurement that the lateral force and the lateral slip were proportional to each other for small slips, and the concept of cornering stiffness (originally named the ‘side-slip’ factor) was introduced. The first investigation into shimmy was even earlier [82], when a two-degree-of-freedom (tramping/roll and shimmy/yaw) model of the front axle of an automobile was studied. The tyres do not play a central roll in this phenomenon, because the two motions are coupled through a gyroscopic moment, hence the term gyroscopic shimmy. More detailed studies of the mechanics of tyres started in the 1940s when the seminal work of von Schlippe and Fromm introduced the basics of the brush and string models, which are related to the concept ‘tyre relaxation’ (or tyre lag) [83]. The role of tyres (and lateral suspension compliance) in shimmy was of great concern, particularly in the context of aircraft landing gear. Many more studies on the challenging topic of tyre dynamics have been published since. A comprehensive treatment of tyres can be found in [8].

In the twenty-first century shimmy phenomena are still reported in motorcycles [84] and bicycles [85, 86], while much attention is devoted to the design of shimmy-free landing gear [87, 88].

This chapter aims to explain the mechanisms and modelling issues related to the generation of tyre forces. Physical models such as the brush and string models are used to clarify the basic concepts. Building upon these findings, the empirical models widespread in vehicle dynamics analyses are discussed. Finally, an overview of some of the advanced models currently used in industry is given.

¹ Shimmy is an oscillation of a wheel around its swivel/steering axis. It is usually called wobble in the context of motorcycle and bicycle dynamics.

3.2 Tyre forces and slips

The tyre makes contact with the road in a contact patch. The interaction between the tyre and the road is described by a force acting on the centre C of the contact patch and a moment; see Figure 3.1. This force and moment are usually described in terms of their (three) components. The tyre force components are the longitudinal force F_x , the cornering (side) force F_y , and the normal force (load) F_z . The three moment components are the overturning couple M_x , the rolling resistance M_y , and the yawing moment M_z .² These forces and moments depend on the tyre's radial deflection δr , its angular velocity Ω , the longitudinal slip κ , the lateral slip α , and the camber angle γ , and the turn slip φ_t (that combine to give the spin slip φ_s).

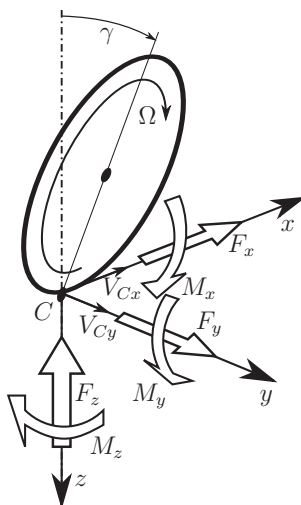


Figure 3.1: Tyre forces and moments.

Since tyres are flexible bodies they have loaded and unloaded radii given by r and r_0 respectively, with the difference given by:

$$\delta r = r_0 - r. \quad (3.1)$$

For a straight-running wheel in free rolling the *effective rolling radius* r_e is defined as:

$$r_e = \frac{V_x}{\Omega_0}, \quad (3.2)$$

where V_x is the velocity of the wheel centre in the x -direction; the wheel's free-rolling angular velocity is Ω_0 . Under these circumstances $V_x = V_{Cx}$; see Figures 3.1 and 3.2.

² It is convenient to define the whole yawing moment as $M_z = M'_z + M''_z$, where M'_z is the component related to the lateral distortion of the tyre contact patch (the only component of a zero-width tyre), while M''_z is the component related to the longitudinal distortion of a finite-width tyre.

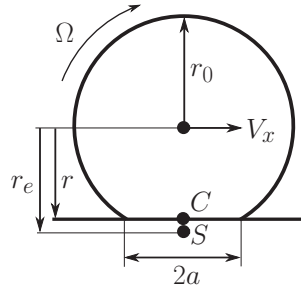


Figure 3.2: Unloaded radius r_0 , loaded radius r , effective radius r_e , point C (centre of the contact patch which has length $2a$), and slip point S .

The wheel is said to be in *free rolling* if it is rolling without the application of a driving or braking torque. In free rolling a small longitudinal (braking) force F_x arises as a result of the rolling resistance moment M_y . The wheel is said to be in a state of *pure rolling* when a driving torque is applied to the wheel that overcomes the rolling resistance moment. As one will appreciate, the unloaded, effective, and loaded radii are related by $r_0 \geq r_e \geq r$; see Figure 3.2. Relationship (3.2) can be used to determine the effective rolling radius by experiment.

In order to define the notion of ‘longitudinal slip’, which is denoted κ , we need to introduce the slip point S . This point is attached to the wheel body at distance r_e from the wheel spindle and forms the centre of rotation when the wheel is in pure rolling; see Figure 3.2. If the wheel is driven, or under braking, the tyre tread begins to ‘slip’ relative to the road with slip velocity:

$$V_{Sx} = V_{Cx} - \Omega r_e, \quad (3.3)$$

where V_{Cx} is the longitudinal velocity of the ground contact point; see Figure 3.1. The longitudinal slip velocity V_{Sx} is positive under braking. The longitudinal slip (or slip ratio) κ is defined as:

$$\kappa = -\frac{V_{Sx}}{V_{Cx}}, \quad (3.4)$$

where κ is negative under braking and $\kappa = -1$ when the wheel is locked. Alternatively,

$$\kappa = \frac{\Omega r_e - V_{Cx}}{V_{Cx}} = \frac{V_r - V_{Cx}}{V_{Cx}} = \frac{V_r}{V_{Cx}} - 1, \quad (3.5)$$

where the rolling velocity V_r and the forward velocity V_{Cx} are related by

$$V_r = \Omega r_e = V_{Cx} - V_{Sx} = V_{Cx}(1 + \kappa). \quad (3.6)$$

The lateral slip $\tan \alpha$ is defined as the ratio of the lateral velocity of point S and the forward velocity of point C :

$$\tan \alpha = -\frac{V_{Sy}}{V_{Cx}}. \quad (3.7)$$

It is often assumed $V_{Sy} \approx V_{Cy}$. In this case the side-slip angle is the angle between the velocity of point C and the wheel’s plane of symmetry. The negative sign is introduced so that positive lateral slips produce positive lateral forces.

The slip velocity components V_{Sx} and V_{Sy} can be combined into a slip vector \mathbf{V}_S given by

$$\mathbf{V}_S = \begin{bmatrix} V_{Sx} \\ V_{Sy} \end{bmatrix}. \quad (3.8)$$

The wheel camber γ is defined as the angle between the wheel diameter through C and a vector normal to the road; see Figure 3.1. It is anticipated that for a car, camber-related lateral forces and moments are much smaller than those related to the lateral slip, since the wheel camber is seldom more than a few degrees. In the case of a motorcycle, however, when the camber can reach values of 50–60 deg, the bulk of the tyre's lateral force is camber related.

The turn slip φ_t is defined as the ratio of the yaw velocity $\dot{\psi}$ and the forward velocity of the contact centre C :

$$\varphi_t = -\frac{\dot{\psi}}{V_{Cx}}. \quad (3.9)$$

This reduces to the path curvature when the lateral slip is zero, since in this case $V_{Cx} = R\dot{\psi}$, where R is the turn radius of curvature. Again, the minus sign is introduced to produce a positive lateral force with a positive turn slip. Turn-slip-related lateral forces and moments are usually only significant for small cornering radii—in parking manoeuvres for example, or when steering from standstill. Turn slip and camber are components of the spin slip φ_s , which is the quantity that is actually related to the force- and moment-generation mechanisms.

The spin slip is defined as the negative ratio of the vertical component of the absolute angular velocity of the wheel ω_z to the forward velocity of the contact centre C :

$$\varphi_s = -\frac{\omega_z}{V_{Cx}}. \quad (3.10)$$

As usual, the minus produces a positive lateral force with a positive spin slip. The angular velocity is related to the yaw rate $\dot{\psi}$, the speed of revolution Ω , and the camber γ via:

$$\omega_z = \dot{\psi} - \Omega \sin \gamma. \quad (3.11)$$

A wheel that experiences zero side slip but both components of spin slip is illustrated in Figure 3.3. Equation (3.10) is thus the sum of two terms, with the first related to the turn slip and the second to the camber:

$$\varphi_s = -\frac{\dot{\psi}}{V_{Cx}} + \frac{\Omega \sin \gamma}{V_{Cx}} = \varphi_t + \frac{\Omega \sin \gamma}{V_{Cx}}. \quad (3.12)$$

In the case that $\alpha = 0$ and $\kappa = 0$ this becomes

$$\varphi_s = \varphi_t|_{\alpha=0} + \frac{\Omega \sin \gamma}{V_{Cx}} \Big|_{\kappa=0} = -\frac{1}{R} + \frac{1}{R_\gamma}, \quad (3.13)$$

where the equivalent camber curvature is given by

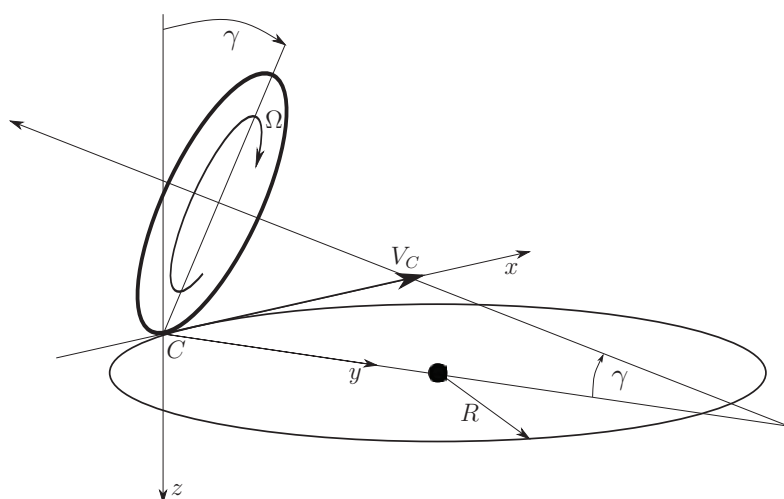


Figure 3.3: Turn-related slip associated with a cambered turning wheel. In this diagram zero lateral slip ($\alpha = 0$) is assumed.

$$\left. \frac{1}{R_\gamma} \right|_{\kappa=0} = \left. \frac{\Omega \sin \gamma}{V_{Cx}} \right|_{\kappa=0} = \frac{1}{r_e} \sin \gamma. \quad (3.14)$$

It follows from (3.13) that the spin slip is zero when $R = R_\gamma$. This occurs when the path curvature matches the curvature of the path taken by the cambered tyre's contact patch through the contact region.

In order to correct for the camber-related curvature arising from the flattening of the tyre contact patch, we introduce the load-induced deflection factor ϵ_γ as follows:

$$\varphi_s = -\frac{\dot{\psi}}{V_{Cx}} + (1 - \epsilon_\gamma) \frac{\Omega \sin \gamma}{V_{Cx}}. \quad (3.15)$$

3.3 Sliding velocities

As the tyre tread rolls into the contact area it will adhere to the road, distort, and generate friction-related ground-contact forces in the plane of the road. When the tread deflection exceeds a limit value it will begin to slide. The contact area is therefore made up typically of adhesion and sliding regions.

In this section we derive expressions for the sliding velocity of an arbitrary tread-base material point in the contact area. These sliding velocities will be used to compute the tyre deflections resulting from slip. The resulting tyre forces and moments can then be found by integration over the contact patch.

The tyre tread behaviour will be analysed with the help of Figure 3.4. The axis system $OXYZ$ is fixed in the road and will be treated as inertial. The Z -axis (not shown) points into the road. The $Cxyz$ coordinate system moves with the wheel and has its origin, C , at the tyre's contact centre. The x - y plane is in the road plane with the z -axis again pointing downwards. The y -axis is the projection of the wheel spindle in the ground plane.

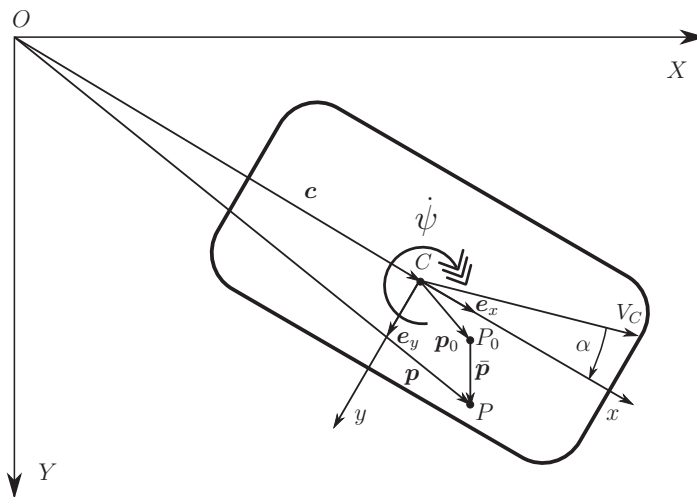


Figure 3.4: Plan view of the tyre contact patch. The vector \mathbf{c} represents the tyre contact centre. The vector \mathbf{p}_0 represents the position of an arbitrary unstressed material point P_0 in the tread base. The friction-related deformation is given by the vector $\bar{\mathbf{p}}$; $\mathbf{p} = \mathbf{c} + \mathbf{p}_0 + \bar{\mathbf{p}}$.

The sliding velocity \mathbf{V}_C will be expressed in the $Cxyz$ coordinate frame and has a longitudinal component V_{Cx} and lateral component V_{Cy} in the \mathbf{e}_x and \mathbf{e}_y directions respectively; see Figure 3.4. The coordinates of the arbitrary stressed material point P (expressed on the $Cxyz$ frame) are $x = x_0 + \bar{x}$ and $y = y_0 + \bar{y}$, where $\mathbf{p}_0 = (x_0, y_0, 0)$ represents the position of an arbitrary unstressed material point, possibly including deformations related to the normal load. The additional deformation $\bar{\mathbf{p}} = (\bar{x}, \bar{y}, 0)$ is induced by tyre–road friction. The absolute Eulerian velocity \mathbf{V}_P of the material point P , expressed in the moving reference frame, is:

$$\mathbf{V}_P = \mathbf{V}_C + \dot{\psi} \mathbf{e}_z \times (\mathbf{p}_0 + \bar{\mathbf{p}}) + (\dot{\mathbf{p}}_0 + \dot{\bar{\mathbf{p}}}) \quad (3.16)$$

or in coordinate form

$$\begin{aligned} V_{Px} &= V_{Cx} - \dot{\psi} (y_0 + \bar{y}) + (\dot{x}_0 + \dot{\bar{x}}) \\ V_{Py} &= V_{Cy} + \dot{\psi} (x_0 + \bar{x}) + (\dot{y}_0 + \dot{\bar{y}}), \end{aligned} \quad (3.17)$$

where V_{Px} is in the \mathbf{e}_x direction and V_{Py} is in the \mathbf{e}_y direction. The first term is related to the translation of the origin of the moving frame, the second term is related to the rotation of the moving frame, and the third term is related to the velocity of the material point within the moving frame.

We will now relate the velocity of P_0 (in the moving reference frame) to the angular velocity of a cambered wheel. Figure 3.5 shows a general point P_0 in the tyre contact area along with the velocity of that point in the moving wheel frame. The kinematic geometry indicates that

$$\begin{aligned} \dot{x}_0 &= -\Omega(r_e - y_0 \sin \gamma) \\ \dot{y}_0 &= -\Omega x_0 \sin \gamma, \end{aligned} \quad (3.18)$$

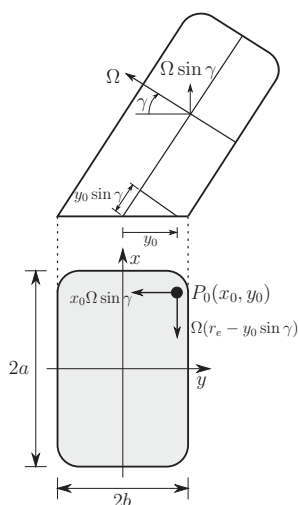


Figure 3.5: Velocity of a general point P_0 in the tyre contact patch.

where Ω is the wheel-spin velocity and r_e the effective rolling radius; $\Omega \sin \gamma$ is a yaw velocity term. In order to accommodate carcass distortion, (3.18) is modified to include a load-induced deflection factor $(1 - \epsilon_\gamma)$ in the camber term $\sin \gamma$.³ In addition x_0, y_0 will be approximated by x, y , since the friction deflections \bar{x}, \bar{y} are assumed ‘small’:

$$\begin{aligned}\dot{x}_0 &= -\Omega(r_e - y(1 - \epsilon_\gamma) \sin \gamma) \\ \dot{y}_0 &= -\Omega x(1 - \epsilon_\gamma) \sin \gamma.\end{aligned}\quad (3.19)$$

When a cambered car tyre makes contact with a frictionless (icy) road, load-induced distortion results in an almost straight contact trajectory, while for a motorcycle tyre the contact trajectory is curved. When cambered tyres roll on real roads (i.e. with friction), the line of contact is almost straight in both cases. In the case of car tyres (almost) no camber-related friction forces arise, since the contact trajectory is approximately straight. With motorcycle tyres, however, camber-related friction forces straighten the contact trajectory.

We will now consider the influence of friction on an arbitrary material point on the tread surface as it rolls into and out of the contact region. The friction-related deformations are given by \bar{x} and \bar{y} in Figure 3.4, and are functions of x_0, y_0 and time. It therefore follows that

$$\begin{aligned}\dot{\bar{x}} &= \frac{d\bar{x}}{dt} = \frac{\partial \bar{x}}{\partial x_0} \dot{x}_0 + \frac{\partial \bar{x}}{\partial y_0} \dot{y}_0 + \frac{\partial \bar{x}}{\partial t} \\ \dot{\bar{y}} &= \frac{d\bar{y}}{dt} = \frac{\partial \bar{y}}{\partial x_0} \dot{x}_0 + \frac{\partial \bar{y}}{\partial y_0} \dot{y}_0 + \frac{\partial \bar{y}}{\partial t}.\end{aligned}\quad (3.20)$$

³ It might be expected that the effect of ϵ_γ on \dot{y}_0 has a significant influence on the tyre’s ability to generate camber-related lateral forces. In the case of a motorcycle tyre $\epsilon_\gamma \approx 0$ (negligible correction), while for car tyres $\epsilon_\gamma \approx 0.5-0.7$ (large correction) resulting in small \dot{y}_0 . These differences relate mainly to the different geometry and structure of motorcycle and car tyres. A large ϵ_γ value is related to the ‘straightening’ of the contact line as a result of the flattening of the loaded tyre.

The second terms in (3.20) are usually much smaller than the other terms and $\partial/\partial x_0$ can be replaced by $\partial/\partial x$ since \bar{x} is small, thus the following approximation will be used from now on:

$$\begin{aligned}\dot{x} &\approx \frac{\partial \bar{x}}{\partial x} \dot{x}_0 + \frac{\partial \bar{x}}{\partial t} \\ \dot{y} &\approx \frac{\partial \bar{y}}{\partial x} \dot{x}_0 + \frac{\partial \bar{y}}{\partial t}.\end{aligned}\quad (3.21)$$

Substituting (3.19) and (3.21) into (3.17), together with $V_{Cx} = V_{Sx} + V_r$, $V_r = r_e \Omega = V_{Cx}(1 + \kappa)$, and the expressions for $\kappa, \alpha, \varphi_s$ given in (3.4), (3.7), (3.15), gives the following expressions for the sliding velocities of a material point in the contact patch that is located at (x, y) :

$$\begin{aligned}V_{Px} &= V_{Cx} - \dot{\psi}y + \dot{x}_0 \left(1 + \frac{\partial \bar{x}}{\partial x}\right) + \frac{\partial \bar{x}}{\partial t} \\ &= V_{Sx} + V_r - y\dot{\psi} + (\Omega y(1 - \epsilon_\gamma) \sin \gamma - V_r) \left(1 + \frac{\partial \bar{x}}{\partial x}\right) + \frac{\partial \bar{x}}{\partial t} \\ &= \frac{\partial \bar{x}}{\partial t} + V_{Sx} + V_{Cx}y\varphi_s - V_r \frac{\partial \bar{x}}{\partial x} \\ &= \frac{\partial \bar{x}}{\partial t} - V_{Cx}\kappa + V_{Cx}y\varphi_s - V_{Cx}(1 + \kappa) \frac{\partial \bar{x}}{\partial x},\end{aligned}\quad (3.22)$$

$$\begin{aligned}V_{Py} &= V_{Cy} + \dot{\psi}x + \dot{y}_0 + \frac{\partial \bar{y}}{\partial x} \dot{x}_0 + \frac{\partial \bar{y}}{\partial t} \\ &= V_{Sy} + x\dot{\psi} - \Omega x(1 - \epsilon_\gamma) \sin \gamma + \frac{\partial \bar{y}}{\partial x} (\Omega y(1 - \epsilon_\gamma) \sin \gamma - V_r) + \frac{\partial \bar{y}}{\partial t} \\ &= \frac{\partial \bar{y}}{\partial t} + V_{Sy} - V_{Cx}x\varphi_s - V_r \frac{\partial \bar{y}}{\partial x} \\ &= \frac{\partial \bar{y}}{\partial t} - V_{Cx} \tan \alpha - V_{Cx}x\varphi_s - V_{Cx}(1 + \kappa) \frac{\partial \bar{y}}{\partial x},\end{aligned}\quad (3.23)$$

where the terms $\partial \bar{x}/\partial x \Omega y(1 - \epsilon_\gamma) \sin \gamma$ and $\partial \bar{y}/\partial x \Omega y(1 - \epsilon_\gamma) \sin \gamma$ have been neglected, because $y, \partial \bar{x}/\partial x, \partial \bar{y}/\partial x$ are assumed ‘small’.

If we now recognize the distance travelled s as the independent variable (rather than time), one obtains

$$s = V_C t \approx V_{Cx} t \xrightarrow{V_{Cx} = \text{const}} ds = V_{Cx} dt. \quad (3.24)$$

The final expressions for the sliding velocity of a point located at (x, y) in the contact patch, which will be used in the development of the string model in Section 3.7, are

$$\begin{aligned}V_{Px} &= \left(\frac{\partial \bar{x}}{\partial s} - \kappa - \left(\frac{\partial \bar{x}}{\partial x}\right)(1 + \kappa) + y\varphi_s\right) V_{Cx} \\ V_{Py} &= \left(\frac{\partial \bar{y}}{\partial s} - \tan \alpha - \left(\frac{\partial \bar{y}}{\partial x}\right)(1 + \kappa) - x\varphi_s\right) V_{Cx}.\end{aligned}\quad (3.25)$$

The steady-state sliding velocities in the contact patch, which will be used in the brush model in Section 3.4, are obtained by assuming that $\partial \bar{x}/\partial s = \partial \bar{y}/\partial s = 0$:

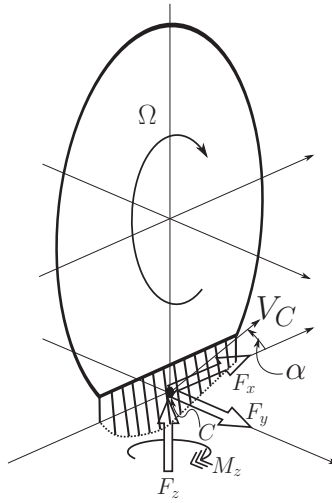


Figure 3.6: Brush model (under pure side slip). The leading and trailing bristles are undeflected; the dotted line represents the deflected contact patch.

$$\begin{aligned} V_{Px} &= \left(-\kappa - \left(\frac{\partial \bar{x}}{\partial x} \right) (1 + \kappa) + y\varphi_s \right) V_{Cx} \\ V_{Py} &= \left(-\tan \alpha - \left(\frac{\partial \bar{y}}{\partial x} \right) (1 + \kappa) - x\varphi_s \right) V_{Cx}. \end{aligned} \quad (3.26)$$

Equations (3.26) show that the velocity field in the contact patch is fully determined by the slips and the position: $(\kappa, \alpha, \varphi_s, x, y) \mapsto (V_{Px}, V_{Py})$. Since the sliding velocities determine the tyre deflections, which result in the tyre forces and moments, κ , α , and φ_s serve as the slip quantities related to the force- and moment-generating mechanisms.

It is noted that the longitudinal slip κ is related to the longitudinal deflection \bar{x} , the lateral slip $\tan \alpha$ is related to the lateral deflection \bar{y} , while both the longitudinal and lateral deflections are related to the spin slip φ_s .

3.4 Steady-state behaviour: the brush model

In this section the ‘brush model’ is used to explain the essentials of steady-state tyre force generation. As shown in Figure 3.6, the brush model consists of a single row of elastic bristles distributed circumferentially around the periphery of a thin disc. As these bristles enter the contact region they are deflected, thereby producing tyre forces and moments; these deflections only occur within the contact patch. The contact patch is assumed to extend between $-a \leq x \leq a$; the rolling resistance is disregarded. When the tyre rolls freely, the tread elements (‘bristles’) remain vertical and move from the leading edge of the contact region to the trailing edge without deflection and without developing any forces. The basic brush model is based on the theory given in [89], with carcass compliance effects included thereafter [90, 91]. The steady-state characteristics of the brush model are analysed in [92]. Asymmetric contact pressure distributions are considered in [93], while more general distributions are reported in [94, 95]. In most cases a parabolic pressure distribution is assumed due to its mathematical simplicity.

3.4.1 Pure side slip

The steady-state deflection in the adhesion region in the case of pure side slip is obtained from (3.26) with $V_{Py} = 0$ (adhesion), and with $\kappa = \varphi_s = 0$ (pure lateral slip)

$$\frac{\partial \bar{y}}{\partial x} = -\tan \alpha \Rightarrow \bar{y} = -x \tan \alpha + c_{\bar{y}}, \quad (3.27)$$

where $c_{\bar{y}}$ is the constant of integration. The boundary condition $\bar{y}(a) = 0$ yields

$$\bar{y}(a) = -a \tan \alpha + c_{\bar{y}} = 0 \Rightarrow c_{\bar{y}} = a \tan \alpha. \quad (3.28)$$

The lateral deflection on the contact patch is therefore given by

$$\bar{y} = (a - x) \tan \alpha = (a - x) \sigma_y, \quad (3.29)$$

where

$$\sigma_y = \tan \alpha. \quad (3.30)$$

Equation (3.29) implies that a tyre material point in full adhesion moves in a straight line once it has entered the contact patch. Note that $\sigma_y = \tan \alpha / (1 + \kappa)$ in the combined slip context—when longitudinal and lateral slipping are present simultaneously—see Section 3.4.4.

The lateral force per unit length of contact patch is related to the lateral stiffness per unit length K_{Py} and the lateral deflection of the tyre, and is given by

$$q_y = K_{Py} \bar{y}. \quad (3.31)$$

The following quadratic force distribution is assumed across the contact region:

$$q_z = \frac{3F_z}{4a} \left\{ 1 - \left(\frac{x}{a} \right)^2 \right\}; \quad (3.32)$$

the normal load is thus given by $F_z = \int_{-a}^{+a} q_z dx$.

The maximum possible local side force is related to the lateral friction coefficient μ_y and local normal load q_z

$$q_y^{\max} = \mu_y q_z, \quad (3.33)$$

while the maximum lateral deflection is

$$\bar{y}_{\max} = \frac{q_y^{\max}}{K_{Py}}. \quad (3.34)$$

As the tread base material enters the contact patch, the strain in the tread material builds up until it reaches a transition point x_t , where adhesion between the rubber and

road transitions into sliding. At the transition point x_t between adhesion and sliding the lateral force is at its maximum, which is given by

$$K_{Py}(a - x_t)|\sigma_y| = \mu_y \frac{3F_z}{4a^3}(a - x_t)(a + x_t). \quad (3.35)$$

Equation (3.35) gives

$$\frac{x_t}{2a} = \frac{2K_{Py}a^2}{3\mu_y F_z}|\sigma_y| - \frac{1}{2} = \theta_{Py}|\sigma_y| - \frac{1}{2}, \quad (3.36)$$

in which the nondimensional tyre parameter θ_{Py} is given by

$$\theta_{Py} = \frac{2K_{Py}a^2}{3\mu_y F_z}. \quad (3.37)$$

Since $x_t \leq a$, it is immediate from (3.36) that

$$|\sigma_y| \leq \frac{1}{\theta_{Py}}. \quad (3.38)$$

This implies that $|\sigma_y| = 1/\theta_{Py}$ corresponds to full sliding.

The tyre side force and aligning moment are now computed by integration across the contact region. The lateral force is split into its adhesion and sliding components, so that $F_y = F_{ya} + F_{ys}$. The adhesion component is given by

$$\begin{aligned} F_{ya} &= \int_{x_t}^a K_{Py} \bar{y} dx = \int_{x_t}^a K_{Py}(a - x)\sigma_y dx \\ &= \frac{K_{Py}\sigma_y}{2}(a - x_t)^2 = 3\mu_y F_z \theta_{Py} \sigma_y (1 - \theta_{Py}|\sigma_y|)^2, \end{aligned} \quad (3.39)$$

while the sliding component is

$$\begin{aligned} F_{ys} &= \int_{-a}^{x_t} \mu_y q_z dx = \int_{-a}^{x_t} \mu_y \frac{3F_z}{4a^3}(a^2 - x^2) dx = \frac{3\mu_y F_z}{4a^3} \left(a^2 x_t + \frac{2a^3}{3} - \frac{x_t^3}{3} \right) \\ &= 3\mu_y F_z \theta_{Py} \sigma_y \left(\theta_{Py}|\sigma_y| - \frac{2}{3}(\theta_{Py}\sigma_y)^2 \right). \end{aligned} \quad (3.40)$$

The full lateral force is obtained by adding (3.39) to (3.40)

$$\begin{aligned} F_y &= F_{ya} + F_{ys} = 3\mu_y F_z \theta_{Py} \sigma_y \left(1 - \theta_{Py}|\sigma_y| + \frac{1}{3}(\theta_{Py}\sigma_y)^2 \right) \\ &= \mu_y F_z \left(\left(\frac{a + x_t}{2a} - 1 \right)^3 + 1 \right) \text{sgn}(\sigma_y). \end{aligned} \quad (3.41)$$

In the case of full sliding ($x_t = a$) (3.41) simplifies to⁴

⁴ Equation (3.41) and (3.45) can only be used for $|\sigma_y| \leq 1/\theta_{Py}$. In the case that $|\sigma_y| > 1/\theta_{Py}$, $F_y = \mu_y F_z \text{sgn}(\sigma_y)$ and $M_z = 0$.

$$F_y = \mu_y F_z \operatorname{sgn}(\sigma_y). \quad (3.42)$$

The yawing moment is computed in terms of its adhesion and sliding components and so $M'_z = M'_{za} + M'_{zs}$, where the adhesion moment is given by

$$\begin{aligned} M'_{za} &= \int_{x_t}^a K_{Py} \bar{y} x dx = \int_{x_t}^a K_{Py} (a - x) \sigma_y x dx \\ &= -\mu_y F_z \theta_{Py} \sigma_y a \left(1 - 6\theta_{Py} |\sigma_y| + 9(\theta_{Py} \sigma_y)^2 - 4(\theta_{Py} |\sigma_y|)^3 \right), \end{aligned} \quad (3.43)$$

while the sliding component is given by

$$\begin{aligned} M'_{zs} &= \int_{-a}^{x_t} \mu_y q_z x dx = \int_{-a}^{x_t} \mu_y \frac{3F_z}{4a^3} (a^2 - x^2) x dx \\ &= -\mu_y F_z \theta_{Py} \sigma_y a \left(3\theta_{Py} |\sigma_y| - 6(\theta_{Py} \sigma_y)^2 + 3(\theta_{Py} |\sigma_y|)^3 \right). \end{aligned} \quad (3.44)$$

The expression for the full moment is obtained by adding (3.43) to (3.44) to obtain:

$$\begin{aligned} M'_z &= -\mu_y F_z \theta_{Py} \sigma_y a \left(1 - 3\theta_{Py} |\sigma_y| + 3(\theta_{Py} \sigma_y)^2 - (\theta_{Py} |\sigma_y|)^3 \right) \\ &= -\mu_y F_z a \left(\frac{a + x_t}{2a} \right) \left(1 - \frac{a + x_t}{2a} \right)^3 \operatorname{sgn}(\sigma_y). \end{aligned} \quad (3.45)$$

The negative sign ensures that the moment opposes the direction of turning, that is, it is an *aligning* moment. In other words, the point at which the lateral force acts is behind the centre of the contact patch. Setting $\frac{\partial M'_z}{\partial x_t} = 0$ gives $x_t = -a/2$, or what is the same $\sigma_y = 1/4\theta_{Py}$ and $|M'_z| = 27/256 = 0.105$.

The pneumatic trail is the distance behind the contact centre at which the resultant side force F_y acts and is computed as

$$\begin{aligned} t &= -\frac{M'_z}{F_y} = a \frac{1 - 3\theta_{Py} |\sigma_y| + 3(\theta_{Py} \sigma_y)^2 - (\theta_{Py} |\sigma_y|)^3}{3 - 3\theta_{Py} |\sigma_y| + (\theta_{Py} \sigma_y)^2} \\ &= a \left(\frac{\left(1 - \left(\frac{x_t + a}{2a} \right) \right)^3}{3 - 3 \left(\frac{x_t + a}{2a} \right) + \left(\frac{x_t + a}{2a} \right)^2} \right). \end{aligned} \quad (3.46)$$

In the case of full sliding $x_t = a$ and so $t = M'_z = 0$. It follows by direct substitution that at peak aligning moment, that is, when $x_t = -a/2$, there obtains $t = 27a/148 = 0.182a$, while at $|\sigma_y| \ll 1$ (where $x_t \approx -a$) it is $t = a/3$.

Figure 3.7 shows the general form of the lateral tyre force, aligning moment, and pneumatic trail generated by the brush model as given in equations (3.41), (3.45), and (3.46) respectively.

The cornering stiffness, aligning moment stiffness, and trail at vanishing slip are computed from (3.41), (3.45), and (3.46) for $\sigma_y \approx \alpha \approx 0$:

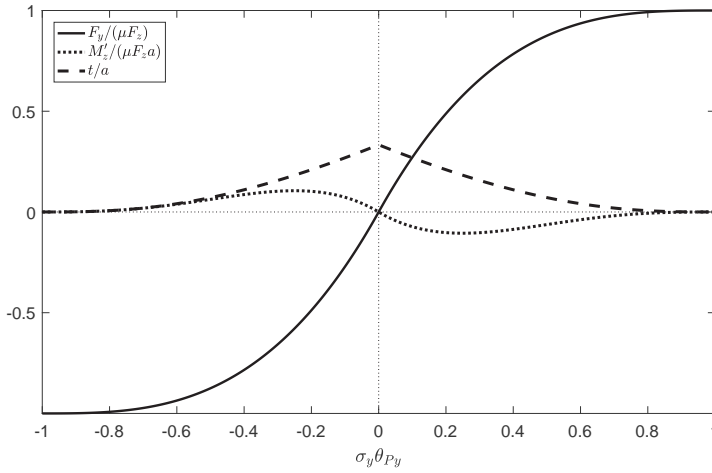


Figure 3.7: Normalized lateral tyre force, aligning moment, and pneumatic trail derived using (3.41), (3.45), and (3.46) respectively.

$$C_{\alpha}^{F_y} = \left. \frac{\partial F_y}{\partial \alpha} \right|_{\alpha=0} = 2K_{Py}a^2 \quad (3.47)$$

$$C_{\alpha}^{M'_z} = - \left. \frac{\partial M'_z}{\partial \alpha} \right|_{\alpha=0} = \frac{2}{3}K_{Py}a^3 \quad (3.48)$$

$$t_0 = \frac{a}{3}. \quad (3.49)$$

It can be reasonably assumed that $a \propto F_z^{1/2}$, resulting in $F_y \propto F_z$ and $M'_z \propto F_z^{3/2}$. In reality, F_y is smaller than $\propto F_z$, because K_{Py} reduces with F_z , and in most cases F_y/F_z and $C_{\alpha}^{F_y}$ have finite maxima; see Section 3.5. Finally, $C_{\alpha}^{F_y}$ and $C_{\alpha}^{M'_z}$ are larger than their measured values, while t_0 is smaller, because the elasticity of the tyre's carcass acts in series with the elasticity of the tread.

3.4.2 Pure longitudinal slip

The steady-state deflection, in the adhesion region in the case of pure longitudinal slip, is obtained from (3.26) with $V_{Px} = 0$ (adhesion assumed), and with $\tan \alpha = \varphi_s = 0$ (pure longitudinal slip assumed),

$$\frac{\partial \bar{x}}{\partial x} = -\frac{\kappa}{1+\kappa} \Rightarrow \bar{x} = -\frac{\kappa}{1+\kappa}x + c_{\bar{x}}, \quad (3.50)$$

where $c_{\bar{x}}$ is a constant of integration. This constant can be computed from the boundary condition $\bar{x}(a) = 0$:

$$\bar{x}(a) = -\frac{\kappa}{1+\kappa}a + c_{\bar{x}} = 0 \Rightarrow c_{\bar{x}} = \frac{\kappa}{1+\kappa}a. \quad (3.51)$$

Therefore the longitudinal deflection on the contact patch is:

$$\bar{x} = (a - x) \frac{\kappa}{1 + \kappa} = (a - x) \sigma_x \quad (3.52)$$

where

$$\sigma_x = \frac{\kappa}{1 + \kappa}. \quad (3.53)$$

All the relationships obtained for the lateral force F_y generated by σ_y , hold valid in the case of the longitudinal force F_x generated from σ_x , mutatis mutandis:

$$\begin{aligned} F_x &= 3\mu_x F_z \theta_{Px} \sigma_x \left(1 - \theta_{Px} |\sigma_x| + \frac{1}{3} (\theta_{Px} \sigma_x)^2 \right) \\ &= \mu_x F_z \left(\left(\frac{x_t + a}{2a} - 1 \right)^3 + 1 \right) \text{sgn}(\sigma_x); \end{aligned} \quad (3.54)$$

where

$$\theta_{Px} = \frac{2K_{Px}a^2}{3\mu_x F_z}. \quad (3.55)$$

The maximum force $F_x = \mu_x F_z$ is again attained in total sliding,⁵ that is, when $|\sigma_x|$ achieves equality in

$$|\sigma_x| \leq \frac{1}{\theta_{Px}}. \quad (3.56)$$

The longitudinal force slip stiffness has a form similar to (3.47), where the longitudinal stiffness per unit length K_{Px} replaces the lateral stiffness K_{Py} :

$$C_\kappa^{F_x} = \left. \frac{\partial F_x}{\partial \kappa} \right|_{\kappa=0} = 2K_{Px}a^2. \quad (3.57)$$

The F_x vs $\sigma_x \theta_{Px}$ characteristic is essentially the same as that in Figure 3.7, when replacing $F_y, \sigma_y, \theta_{Py}$ with $F_x, \sigma_x, \theta_{Px}$.

3.4.3 Pure spin slip

The steady-state deflection in the adhesion region in the case of pure spin slip is obtained from (3.26) with $V_{Px} = V_{Py} = 0$, and with $\tan \alpha = \kappa = 0$

$$\frac{\partial \bar{x}}{\partial x} = y \varphi_s \Rightarrow \bar{x} = y x \varphi_s + c_{\bar{x}} \quad (3.58)$$

$$\frac{\partial \bar{y}}{\partial x} = -x \varphi_s \Rightarrow \bar{y} = -\frac{x^2}{2} \varphi_s + c_{\bar{y}} \quad (3.59)$$

where $c_{\bar{x}}$ and $c_{\bar{y}}$ are constants of integration related to the boundary conditions $\bar{x}(a) = 0$ and $\bar{y}(a) = 0$

⁵ Equation (3.54) can only be used for $|\sigma_x| \leq 1/\theta_{Px}$. In the case that $|\sigma_x| > 1/\theta_{Px}$, $F_x = \mu_x F_z \text{sgn}(\sigma_x)$.

$$\bar{x}(a) = ya\varphi_s + c_{\bar{x}} = 0 \Rightarrow c_{\bar{x}} = -ya\varphi_s \quad (3.60)$$

$$\bar{y}(a) = -\frac{a^2}{2}\varphi_s + c_{\bar{y}} = 0 \Rightarrow c_{\bar{y}} = \frac{a^2}{2}\varphi_s. \quad (3.61)$$

Therefore the longitudinal and lateral deflections in the contact patch are

$$\bar{x} = -y(a-x)\varphi_s \quad (3.62)$$

$$\bar{y} = \frac{1}{2}(a^2 - x^2)\varphi_s. \quad (3.63)$$

Equation (3.63) implies that a tyre material point in adhesion moves along a circle of radius R in pure turn slip, and along a straight line in pure camber.⁶

In pure camber

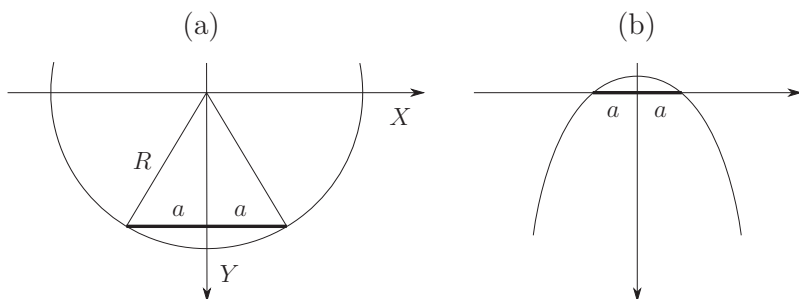
$$\bar{y} = -y_{\gamma 0} = \frac{1}{2}(a^2 - x^2)\frac{(1 - \epsilon_{\gamma})}{r_e} \sin \gamma, \quad (3.64)$$

which is the friction-related deflection in the adhesion region, or what is the same, the bristle contact line for a cambered tyre on a frictionless surface.

The force and moment resulting from φ_s will again be computed by integration over the adhesion and sliding regions. In the case that both adhesion and sliding occur, the analysis is more complicated. We will therefore consider the case of pure adhesion first in order to gain insight into the basic characteristics of the camber and turn slip force- and moment-generation mechanisms. While this is clearly an approximation, we make a ‘thin tyre’ approximation in the more general case in which both adhesion and sliding occur.

⁶ (a) In pure turn slip $\varphi_s = -1/R$ and the distance between a circle of radius R and the straight-line segment of length $2a$ at $Y = R\sqrt{1 - (a/R)^2}$, the line of contact on a frictionless surface, is:

$$R\sqrt{1 - (a/R)^2} - R\sqrt{1 - (x/R)^2} \approx R\left(1 - \frac{1}{2}\left(\frac{a}{R}\right)^2\right) - R\left(1 - \frac{1}{2}\left(\frac{x}{R}\right)^2\right) = \frac{1}{2}(a^2 - x^2)\frac{-1}{R}.$$



(b) In pure camber $\varphi_s = \frac{(1 - \epsilon_{\gamma})}{r_e} \sin \gamma$ and the distance between the line of contact of a straight-running cambered tyre on a frictionless surface and the straight-line segment of length $2a$ is found by integration of \dot{y}_0 in (3.19) using the transformation $\dot{y}_0 = \frac{dy_0}{dx} \frac{dx}{dt} = \frac{dy_0}{dx} (-\Omega r_e)$:

$$\int_{-a}^x \frac{1}{-\Omega r_e} (-\Omega \hat{x} (1 - \epsilon_{\gamma}) \sin \gamma) d\hat{x} = \frac{1}{2}(x^2 - a^2) \frac{(1 - \epsilon_{\gamma})}{r_e} \sin \gamma = -\frac{1}{2}(a^2 - x^2)\varphi_s = y_{\gamma 0}.$$

In the case of full adhesion, the lateral deflection \bar{y} given in (3.63) is symmetrical around the centre of the contact region and will thus not contribute to the yawing moment. The lateral force is obtained by integrating over the contact patch (of length $2a$ and width $2b$); only the lateral deflections contribute to the lateral force

$$\begin{aligned} F_y &= \int_{-a}^{+a} \int_{-b}^{+b} \frac{K_{Py}}{2b} \bar{y} dy dx = \iint \frac{K_{Py}}{2b} \frac{1}{2} (a^2 - x^2) \varphi_s dy dx \\ &= \frac{2}{3} K_{Py} a^3 \varphi_s. \end{aligned} \quad (3.65)$$

The z -axis moment is also obtained by integration over the contact patch. As one would expect by symmetry, only the longitudinal deflections contribute to the moment

$$\begin{aligned} M_z^r &= - \int_{-a}^{+a} \int_{-b}^{+b} \frac{K_{Px}}{2b} \bar{x} y dy dx = \iint \frac{K_{Px}}{2b} y^2 (a - x) \varphi_s dy dx \\ &= \frac{2}{3} K_{Px} a^2 b^2 \varphi_s. \end{aligned} \quad (3.66)$$

Despite their simplicity, there are a number of points that are worth making in connection with (3.65) and (3.66). Since the spin slip has a positive camber-related term and a negative turn-slip-related term, F_y and M_z^r can change direction according to which of these terms is dominant. If the turn-slip-related term is dominant, the side force F_y in (3.65) is negative, and thus directed away from the centre of path curvature; see Figure 3.3. This force therefore tends to ‘straighten up’ the tyre’s ground-plane trajectory. A turn-slip-dominant moment in (3.66) is negative and will thus also act to ‘straighten up’ the tyre’s ground-plane trajectory. In the camber-dominant case, the spin slip will increase the tyre’s path curvature (misaligning moment). In the pure adhesion case the spin-slip-related force is proportional to φ_s , while the spin-slip-related moment vanishes in the limit $b \rightarrow 0$. Note that sometimes (3.65) and (3.66) are derived using the longitudinal and lateral stiffness per unit area K'_{Px} and K'_{Py} , instead of the longitudinal and lateral stiffnesses per unit length $K_{Px} = K'_{Px} 2b$ and $K_{Py} = K'_{Py} 2b$ used herein.

The spin-slip-force stiffness and moment stiffness are:

$$C_{\varphi_s}^{F_y} = \left. \frac{\partial F_y}{\partial \varphi_s} \right|_{\varphi_s=0} = \frac{2}{3} K_{Py} a^3 = C_{\alpha}^{M'_z} \quad (3.67)$$

$$C_{\varphi_s}^{M_z^r} = \left. \frac{\partial M_z^r}{\partial \varphi_s} \right|_{\varphi_s=0} = \frac{2}{3} K_{Px} a^2 b^2. \quad (3.68)$$

It is noted that the spin-slip lateral force stiffness $C_{\varphi_s}^{F_y}$ in (3.67) is the same as the aligning moment lateral slip stiffness $C_{\alpha}^{M'_z}$ in (3.48). This reciprocity property is lost when spin-induced lateral slip resulting from the yaw compliance of the tyre is considered [96]; see also Section 3.4.6 for a discussion on induced/apparent slips.

The force and moment can be rewritten to separate explicitly the contributions of turn slip φ_t (or curvature $1/R$) and camber γ . Using (3.15) gives

$$\begin{aligned}
F_y &= C_{\varphi_s}^{F_y} \left(\varphi_t + \frac{1-\epsilon_\gamma}{r_e} \sin \gamma \right) \Big|_{\alpha=0} = -C_{\varphi_s}^{F_y} \left(\frac{1}{R} - \frac{1-\epsilon_\gamma}{r_e} \sin \gamma \right) \\
M_z^r &= C_{\varphi_s}^{M_z^r} \left(\varphi_t + \frac{1-\epsilon_\gamma}{r_e} \sin \gamma \right) \Big|_{\alpha=0} = -C_{\varphi_s}^{M_z^r} \left(\frac{1}{R} - \frac{1-\epsilon_\gamma}{r_e} \sin \gamma \right).
\end{aligned}
\tag{3.69}$$

Experimental tests [96] suggest that $\epsilon_\gamma \approx 0.5-0.7$ for radial ply car tyres. This has the effect of introducing a factor of 2 to 3 between the road curvature- and camber-related terms in (3.69);⁷ this observation is supportive of the discussion following (3.19).

The influence of spin-related sliding is now considered. If we again invoke the quadratic pressure distribution (3.32), the lateral stiffness (3.31), and the lateral strain displacement (3.63), there holds

$$K_{Py} \frac{1}{2} (a^2 - x^2) \varphi_s^{sl} = \mu_y \frac{3F_z}{4a^3} (a^2 - x^2)$$

and so the spin slip on the limit of sliding is given by

$$\varphi_s^{sl} = \frac{3\mu_y F_z}{2K_{Py} a^3} = \frac{1}{a\theta_{Py}}. \tag{3.70}$$

If one substitutes φ_s^{sl} into (3.65) there obtains $F_y = \mu_y F_z$. Note that (3.70) resembles (3.38) and (3.56) for lateral and longitudinal slips under conditions of full sliding. However, in this case it is anticipated that for $|\varphi_s| > \varphi_s^{sl}$ only the front half of the patch and the trailing edge are sliding, while full sliding occurs only when $|\varphi_s| \rightarrow \infty$ (a tyre steered from standstill); see the remark following (3.74).

The analysis of spin-slip sliding in the case of a two-dimensional tyre tread base model is complicated [8]. For that reason we will now analyse the side-force- and moment-generation process related to spin slip using the ‘thin’ brush-type tyre model. In this model the side force is generated by the lateral deflections \bar{y} given in (3.31) and the parabolic pressure distribution (3.32). Since both the lateral deflection (3.63) and the pressure distribution are parabolic, no sliding will occur for $\varphi_s \leq \varphi_s^{sl}$, with the adhesion limit then reached throughout the contact patch.

To analyse the sliding case we make use of Figure 3.8. For $\varphi_s > \varphi_s^{sl}$ all material points on the front half of the contact patch ($0 < x < a$) slide simultaneously. The contact line is dictated by the maximum lateral deflection at the limit of adhesion. It follows from (3.32), (3.33), and (3.34) that

$$\bar{y}^{\max} = \frac{q_y^{\max}}{K_{Py}} = \frac{3}{4} \mu_y F_z \frac{a^2 - x^2}{a^3} \frac{1}{K_{Py}} = \frac{a^2 - x^2}{2a\theta_{Py}} \tag{3.71}$$

with θ_{Py} defined in (3.37).

In the case of pure turn slip (Figure 3.8(a)) the bristles move away from $y = 0$, which would be their position on a frictionless surface, to $y = \bar{y}^{\max}$. In the case of pure

⁷ The parameter ϵ_γ can be computed from $(1 - \epsilon_\gamma)/r_e = C_\gamma^{F_y}/C_{\varphi_t}^{F_y}$, since $C_\gamma^{F_y} = C_{\varphi_s}^{F_y}(1 - \epsilon_\gamma)/r_e$ and $C_{\varphi_t}^{F_y} = C_{\varphi_s}^{F_y}$.

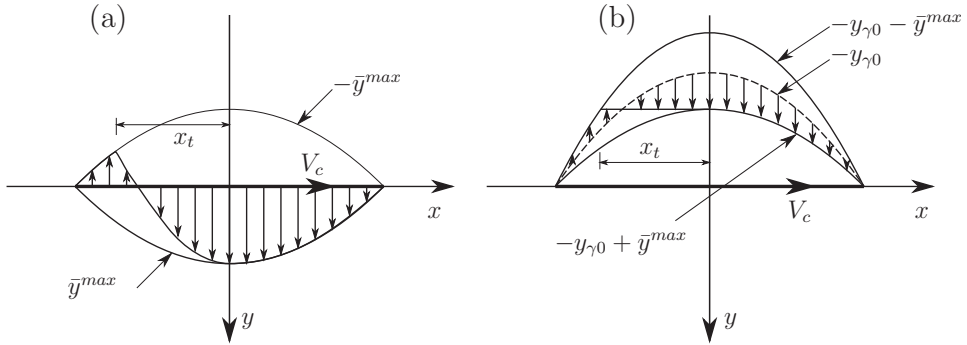


Figure 3.8: Tread deformation for a ‘thin’ brush model under pure turn slip (a), or pure camber (b) [8]. The curves $y_{\gamma 0}$ and \bar{y}^{max} are given in (3.64) and (3.71) respectively.

camber (Figure 3.8 (b)) the bristles move away from $y = -y_{\gamma 0}$, which would be their position on a frictionless surface, to $y = -y_{\gamma 0} + \bar{y}^{max}$. Once the contact line reaches the rear half of the contact region, sliding ceases and adhesion resumes. The reason for this is that friction forces constrain the tread base material to follow a curved path in the case of pure turn slip, and a straight line in the case of pure camber whenever the friction limit is not exceeded; see comment following (3.63). In the rear half of the contact region the bristle deflection \bar{y} reduces from its maximum value of $\bar{y}^{max} = a^2/2a\theta_{Py} = \frac{1}{2}a^2\varphi_s^{sl}$ at the centre of the contact patch, and adhesion is re-established; see Figure 3.8. Therefore, in pure turn slip, the tread material switches from the \bar{y}^{max} boundary to the $-\bar{y}^{max}$ boundary (with the curvature dictated by φ_t), where the friction limit is once again reached. In the case of pure camber, the tread base material moves to the $-y_{\gamma 0} - \bar{y}^{max}$ boundary, where the friction limit is again reached. In both cases the trailing edge is sliding in the opposite direction (as compared with the sliding in the front half of the contact patch). It is clear that for $\varphi > \varphi_{sl}$ a moment M'_z must be generated, because the deflection \bar{y} is no longer symmetric and F_y reduces, because of the sign change in the trailing edge deflection.

We now need to find the transition point x_t at which sliding is re-established. To do this we must respect the maximal deflection constraint (3.71) at $x = 0$ and allow the sliding region to cross from the $+\bar{y}^{max}$ boundary to the $-\bar{y}^{max}$ boundary (pure turn slip), or from $-y_{\gamma 0} + \bar{y}^{max}$ to $-y_{\gamma 0} - \bar{y}^{max}$ (pure camber), whenever $\varphi_s > \varphi_s^{max}$. Following (3.63) and (3.71)

$$\bar{y}_{x_t \leq x \leq 0} = \frac{1}{2}a^2\varphi_s^{sl} - \frac{1}{2}x^2\varphi_s \quad (3.72)$$

which gives (using (3.71))

$$\frac{1}{2}a^2\varphi_s^{sl} - \frac{1}{2}x_t^2|\varphi_s| = -\frac{a^2 - x_t^2}{2a\theta_{Py}} \quad (3.73)$$

and so

$$\frac{x_t}{2a} = \frac{-1}{\sqrt{2(1 + a\theta_{Py}|\varphi_s|)}}. \quad (3.74)$$

The negative root has been selected, because the transition point is on the rear half of the contact patch. Note that when $|\varphi_s| = \varphi_s^{sl}$ $x_t = -a$, and when $|\varphi_s| \rightarrow \infty$ $x_t = 0$.

The contact force is now computed by integration over the three sections of the contact patch: sliding trailing edge (I), adhesion rear half (II), and sliding front half (III)

$$\begin{aligned} F_y^I &= - \int_{-a}^{x_t} K_{Py}(\bar{y}^{\max}) dx = -K_{Py} \int_{-a}^{x_t} \frac{a^2 - x^2}{2a\theta_{Py}} dx = -\frac{K_{Py}}{6a\theta_{Py}} (2a^3 + 3a^2x_t - x_t^3) \\ F_y^{II} &= \int_{x_t}^0 K_{Py} \frac{1}{2} (a^2\varphi_s^{sl} - x^2\varphi_s) dx = \frac{K_{Py}x_t}{6} \left(x_t^2\varphi_s - \frac{3a}{\theta_{Py}} \right) \\ F_y^{III} &= \int_0^a K_{Py}\bar{y}^{\max} dx = \frac{1}{2}\mu_y F_z. \end{aligned}$$

The whole lateral force is obtained by adding the three components above and introducing θ_{Py} and x_t from (3.37) and (3.74):

$$F_y = F_y^I + F_y^{II} + F_y^{III} = \mu_y F_z \sqrt{2} \frac{1}{\sqrt{1 + a\theta_{Py}|\varphi_s|}}. \quad (3.75)$$

Similarly, the moment is obtained by integration on the same three sections

$$\begin{aligned} M_z^I &= - \int_{-a}^{x_t} K_{Py}(\bar{y}^{\max}) x dx = \frac{K_{Py}}{8a\theta_y} (a^2 - x_t^2)^2 \\ M_z^{II} &= \int_{x_t}^0 K_{Py} \frac{1}{2} (a^2\varphi_s^{sl} - x^2\varphi_s) x dx = -\frac{K_{Py}x_t^2}{4\theta_{Py}} \left(a - \frac{1}{2}\theta_{Py}x_t^2\varphi_s \right) \\ M_z^{III} &= \int_0^a K_{Py}\bar{y}^{\max} x dx = \frac{3}{16}a\mu_y F_z. \end{aligned}$$

The full moment is obtained by adding the three components above and introducing θ_{Py} and x_t from (3.37) and (3.74):

$$M'_z = M_z^I + M_z^{II} + M_z^{III} = \frac{3}{8}\mu_y F_z a \frac{a\theta_{Py}|\varphi_s| - 1}{a\theta_{Py}|\varphi_s| + 1} \text{sgn}(\varphi_s). \quad (3.76)$$

The general form of (3.75) and (3.76) is shown in Figure 3.9.⁸ It is clear that the side force grows linearly in the adhesion region, reaching a peak at the limit of sliding; after that it decays away as a result of opposing force contributions either side of the transition point x_t . As predicted in (3.66), M'_z is zero in the adhesion region, with the moment growing after that as a result of the unbalanced forces distribution across the contact patch under sliding. The force and moment as the spin approaches infinity can be determined by allowing $|\varphi_s| \rightarrow \infty$ in (3.75) and (3.76):

$$F_y = 0 \quad M_z^{\max} = \frac{3}{8}\mu_y F_z a. \quad (3.77)$$

In this case $x_t = 0$ which results in the rear half of the contact patch sliding in the opposite direction to the front half; see Figure 3.8.

⁸ Equations (3.75) and (3.76) can only be used for $|\varphi_s| \geq \varphi_s^{sl}$, while at lower values of $|\varphi_s|$ (3.65) and (3.66) hold.

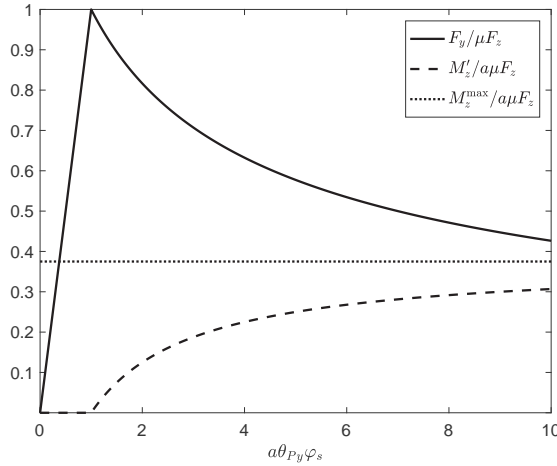


Figure 3.9: Normalized spin-slip-related force and moment for a ‘thin’ brush model, derived using (3.65), (3.66), (3.75), and (3.76).

It is interesting to note that experimental studies suggested a similar behaviour [91]

$$M_z^{\max} = \frac{3}{8}\mu F_z \left(a + \frac{2}{3}b \right), \quad (3.78)$$

where the additional term is related to the contact patch width; recall that the derivation of (3.77) was carried out using a ‘thin’ brush model. In general, the accurate modelling of the behaviour at standstill is not trivial.

In sum, for spin slip up to φ_s^{sl} , the moment is related only to the longitudinal deflection \bar{x} , $M_z = M'_z$, which is misaligning in the case of pure camber and aligning in the case of pure turn slip. Above the sliding limit φ_s^{sl} an additional moment M'_z is generated that arises from the lateral deflection \bar{y} (again misaligning in the case of pure camber and aligning in the case of pure spin slip). The force F_y is related to the lateral deflection \bar{y} only and increases with the spin slip up to φ_s^{sl} . It then reduces and is zero at large spin slip, where the moment attains its maximum value.

3.4.4 Combined lateral and longitudinal slip

We will assume for simplicity that $K_P = K_{Px} = K_{Py}$, $\mu = \mu_x = \mu_y$, and $\theta_p = \theta_{Px} = \theta_{Py}$. The velocities of tread-base material points in the contact region are given by $V_r = \Omega r_e$. Equations (3.52) and (3.29) give the relationship between the longitudinal tread deflection \bar{x} and the lateral tread deflection \bar{y} , with the theoretical slips σ_x and σ_y given by

$$\begin{bmatrix} \bar{x} \\ \bar{y} \end{bmatrix} = (a - x) \begin{bmatrix} \sigma_x \\ \sigma_y \end{bmatrix}, \quad (3.79)$$

where the relationships between the theoretical and practical slip quantities are

$$\sigma_x = \frac{\kappa}{1 + \kappa} \quad \sigma_y = \frac{\tan \alpha}{1 + \kappa} \quad (3.80)$$

according to (3.53) and (3.30)⁹ respectively.

Equation (3.79) highlights the idea that the tyre deflections are governed independently by σ_x and σ_y (and not by κ and $\tan \alpha$).

The transition point can be computed in the same way it was in the case of pure lateral force by introducing σ in place of σ_y (compare with (3.35))

$$K_P(a - x_t)\sigma = \mu \frac{3F_z}{4a^3}(a - x_t)(a + x_t) \quad (3.81)$$

where

$$\sigma = \sqrt{\sigma_x^2 + \sigma_y^2} \quad (3.82)$$

to obtain

$$\frac{x_t}{2a} = \theta_P \sigma - \frac{1}{2}, \quad (3.83)$$

which can be compared with (3.36). Again full sliding ($x_t = +a$) occurs for $\sigma \geq 1/\theta_P$. The expressions for the force, aligning moment, and pneumatic trail are found in the same way:

$$\begin{bmatrix} F_x \\ F_y \end{bmatrix} = \frac{F}{\sigma} \begin{bmatrix} \sigma_x \\ \sigma_y \end{bmatrix} \quad (3.84)$$

where

$$F = 3\mu F_z \theta_P \sigma \left(1 - \theta_P \sigma + \frac{1}{3} (\theta_P \sigma)^2 \right) \quad \text{if } \sigma \leq 1/\theta_P \quad (3.85)$$

$$= \mu F_z \quad \text{if } \sigma > 1/\theta_P \quad (3.86)$$

$$M'_z = -tF_y \quad (3.87)$$

$$t = a \frac{1 - 3\theta_P \sigma + 3(\theta_P \sigma)^2 - (\theta_P \sigma)^3}{3 - 3\theta_P \sigma + (\theta_P \sigma)^2}. \quad (3.88)$$

Note that the isotropic stiffness and friction assumptions mean that the deflection is in the direction opposite to the slip vector \mathbf{V}_s .

Figure 3.10 illustrates a key feature of the coupling between the longitudinal and lateral forces, which is that the generation of one comes at the expense of the other. Figure 3.10 (a) shows how the lateral force F_y , at a fixed side-slip angle α , drops away when the tyre is asked simultaneously to generate braking or driving forces ($|F_y| \rightarrow 0$ when $\kappa \rightarrow \infty$). Figure 3.10 (b) shows how the longitudinal force F_x , at a fixed side-slip angle κ , drops away when the tyre is asked simultaneously to generate a side

⁹ It can be shown that a theoretical slip of $\sigma_y = \frac{\tan \alpha}{1 + \kappa}$ is obtained in place of $\sigma_y = \tan \alpha$ when integrating (3.26) under the assumption of constant κ rather than $\kappa = 0$.

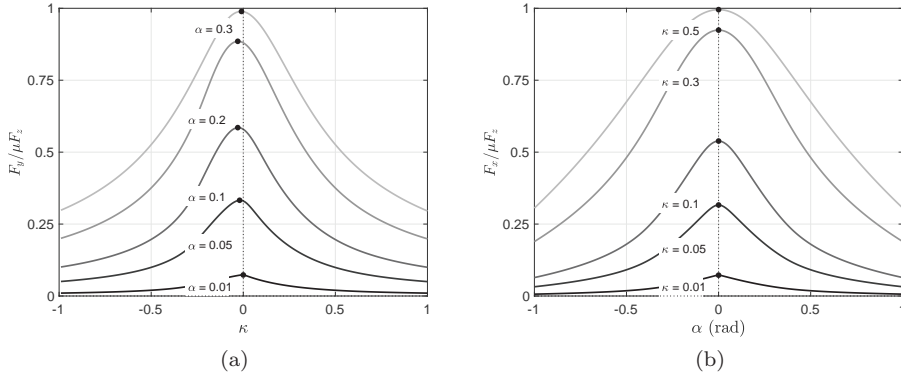


Figure 3.10: The influence of combined slip in the simple brush model. Graph (a) shows the normalized lateral force, for various fixed values of side-slip angle α , as a function of the longitudinal slip κ . Graph (b) shows the normalized longitudinal force, for various fixed values of longitudinal slip κ , as a function of α .

force ($|F_x| \rightarrow 0$ when $|\tan \alpha| \rightarrow \infty$, that is, $|\alpha| \rightarrow \pi/2$). It will be observed that the peak of the side force characteristic in Figure 3.10 (a) is biased towards the braking abscissa.¹⁰ Experimental evidence shows that often the shape of these curves is even more asymmetric than predicted by the brush model. Possible reasons are increased contact length during braking and brake force-induced slip angle.

The spin-slip effect can be included in the present formulation by replacing the side slip $\tan \alpha$ in (3.80) with $\tan \alpha^*$, where

$$\alpha^* = \alpha + \frac{C_{\varphi_s}^{F_y}}{C_{\alpha}^{F_y}} \varphi_s \quad (3.89)$$

has the actual side-slip angle and an equivalent side-slip angle representing the effect of spin slip. The residual moment $M_z^r = C_{\varphi_s}^{M_z^r} \varphi_s$ can also be added to the aligning moment M_z' in (3.87) to give the total yawing moment

$$M_z = M_z' + M_z^r. \quad (3.90)$$

3.4.5 Combined lateral, longitudinal, and spin slip

As with all analytic physics-based models, at some point they become too complex to be practically useful. In particular, the brush model discussed cannot realistically be used to treat combined lateral, longitudinal, and spin slip, especially if one wishes also

¹⁰ Figure 3.10 (a) is asymmetric, because σ_y varies asymmetrically in κ (for fixed α); $\sigma_y \propto 1/(1 + \kappa)$ which increases under braking and decreases under driving. In addition, σ_x is asymmetric in κ . Figure 3.10 (b) is symmetric; because σ_x is constant for constant κ , variations in α only affect σ_y , and $\sigma_y(\alpha) = -\sigma_y(-\alpha)$.

to accommodate arbitrary pressure distributions, non-isotropic stiffness and friction properties, and finite tread widths. One may, however, consider using numerical models such as *TreadSim* [8] in more complex situations.

In practice, vehicle simulation models usually use an empirical tyre model such as those reported in Section 3.5. The parameters that populate these models are derived from experimental tests using various tyre-testing machines such as test trailers (e.g. TNO Tyre Test Trailer), flat-track test machines (e.g. MTS Flat Trac, Calspan TIRF), flat-plank testers (e.g. [97]), flat-disk machines (e.g. [98]), and internal or external drum test machines (e.g. [99]).

3.4.6 Summary of analytical models

The role of physics-based models, such as the brush model described earlier in this chapter, is to uncover the basic tyre force- and moment-generating mechanisms. Both quantities arise as a result of friction-induced tread material distortion and sliding, as quantified by the longitudinal slip κ , the lateral slip $\tan \alpha$, and the spin slip φ_s . For small values of slip, the forces and moments are proportional to slip. The constants of proportionality are the slip stiffnesses $C_{\kappa}^{F_x}$, $C_{\alpha}^{F_y}$, $C_{\varphi_s}^{F_y}$, $C_{\alpha}^{M_z}$, and $C_{\varphi_s}^{M_z}$, which can be either computed or measured. Under small-slip conditions the majority of the contact patch is in adhesion, with tread material sliding only a minor influence. As the slip increases, so does sliding. Under increased slip conditions the relationships with the resulting forces and moments become increasingly nonlinear until saturation occurs. In the above analysis we have seen that full-patch sliding can occur in pure side slip when $F_y = \mu_y F_z \text{sgn}(\sigma_y)$; that full-patch sliding can occur in pure longitudinal slip when $F_x = \mu_x F_z \text{sgn}(\sigma_x)$; and that full-patch sliding can occur in pure spin slip when $F_y = 0$ and $M_z = \frac{3}{8} \mu_y F_z a$.

Numerical simulations can be found in [8] which go well beyond the capabilities of the brush models discussed here. These include such things as a sliding-velocity-dependent friction coefficient, a flexible tyre carcass, a finite tread width ($b > 0$), and combined lateral and spin slip. In the case of a friction coefficient that decreases with velocity, the tyre forces exhibit a peak that is found in most experimental testing. If the tyre has a flexible carcass, a reduction in the slip stiffness is expected and observed, which is the result of the tyre’s reduced structural stiffness. The flexible carcass also causes an increase in the pneumatic trail. When spin slip is present, the yaw compliance of the tyre combined with the finite width of the contact patch leads to a force-induced side slip which increases $C_{\varphi_s}^{F_y}$ (and reduces $C_{\varphi_s}^{M_z}$). This effect is also related to the loss of the reciprocity property ($C_{\varphi_s}^{F_y} = C_{\alpha}^{M_z}$), which is experimentally observed. Finally, the yaw compliance causes an apparent side slip which increases/decreases the camber-related side force when braking/accelerating.

3.5 Steady-state behaviour: the ‘magic formula’

The dominant tyre model currently in use is the so called magic formula model. This is an empirical parametric model that has its parameter values optimized to fit experimentally measured steady-state tyre force and moment data. magic formula models

provide an accurate representation of the experimental data, but with a model complexity much lower than that required of physics-based models of similar accuracy. The cost of this modelling approach is the loss of physical insight combined with non-physical parameters. The model formulae are usually functions of the normal load and more recently the inflation pressure. A number of scaling factors are used to extrapolate the model's behaviour to conditions away from those of the original testing.

The development of the magic formula tyre model began in the late 1980s [100–102]. The physics-based approach to combined slip conditions is used in this work. In later versions of the magic formulae, the friction circle is replaced by an empirical formula introduced by Michelin [103]. The effect of inflation pressure was introduced explicitly into the formula in [104]. There are still some important influences, such as temperature, which are not currently represented. That said, some of the manufacturers have developed temperature-dependent magic formulae. The aim of this section is to discuss the key features of these models, without going into all the ins and outs of the various different versions of the magic formula models. Once an overview understanding is obtained, it is relatively easy to move between different versions and upgrades; widely used versions are reported in [105] and [106], with a motorcycle version available in [107]. The latest version is reported in [8], which is essentially the same as that reported in [104], which can be downloaded from the Internet.¹¹

The brush model analysis given in Section 3.4 showed that the tyre force and moment depend predominantly on the longitudinal slip κ , the lateral slip $\tan \alpha$, the spin slip φ_s , and vertical load F_z . The magic formulae will therefore have these quantities as inputs. Under most circumstances, only the camber component of the spin slip is important and so the most widespread versions of the magic formula use the camber γ instead of the more general spin slip φ_s .

3.5.1 Pure slip

The basic magic formula for the pure longitudinal force is:

$$F_x = D_x \sin(C_x \arctan(B_x \kappa - E_x(B_x \kappa - \arctan(B_x \kappa)))) \quad (3.91)$$

in which B_x is the stiffness factor, C_x is the shape factor, and E_x is the curvature factor. If $C_x > 1$, $D_x = \mu_x F_z$ gives the peak value of F_x ; μ_x is the friction coefficient for longitudinal forces. If $E_x < 1$, $F_x > 0$ when $\kappa \rightarrow +\infty$. The curve given in (3.91) passes through the origin ($F_x(0) = 0$) and has slope $B_x C_x D_x$ there, which corresponds to the longitudinal slip stiffness $C_\kappa^{F_x}$ estimated in (3.57). The peak force is D_x (assuming $C_x > 1$) and then saturates at:

$$\lim_{\kappa \rightarrow \infty} F_x = \begin{cases} D_x \sin(C_x \pi/2) \operatorname{sgn}(1 - E) \operatorname{sgn}(B) & E \neq 1 \\ D_x \sin(C_x \arctan(\pi/2)) \operatorname{sgn}(B) & E = 1. \end{cases} \quad (3.92)$$

If B_x , C_x , D_x , and E_x are constant, the magic formula (3.91) generates an anti-symmetric curve. It then reaches a maximum/minimum and subsequently tends towards horizontal asymptotes. One may wish to introduce offsets to this curve in order

¹¹ See <http://www.mate.tue.nl/mate/pdfs/11281.pdf>.

to accommodate such things as rolling resistance ($F_x \neq 0$ when $\kappa = 0$ —see the free-rolling convention in Section 3.2). This can be achieved by replacing κ with $\kappa + S_H$ and/or F_x with $F_x + S_V$ for example. Setting $S_H = -M_y/(rB_xC_xD_x)$, which gives $F_x(0) = -M_y/r$, where M_y is the rolling resistance moment. Alternatively, if $S_H = 0$, $S_V = -M_y/r$ also gives $F_x(0) = -M_y/r$.

In the standard case that $C_x > 1$ and $E_x < 1$ the parameters can be determined as follows: D_x is obtained from the peak value $D_x = F_x^{\max}$; C_x is obtained from the asymptote $F_x^\infty = \lim_{\kappa \rightarrow \infty} F_x$, since $C_x = 2 \arcsin(F_x^\infty/D_x)/\pi$ —see (3.92); B_x is obtained from the slope at the origin, since $B_x = \partial F_x / \partial \kappa|_{\kappa=0} / C_x D_x$ (hence stiffness parameter); and finally E_x is obtained from $E_x = (B_x \kappa_m - \tan(\pi/2C_x)) / (B_x \kappa_m - \arctan(B_x \kappa_m))$ where κ_m corresponds to the position of the peak. In practice the parameters are determined using nonlinear fitting algorithms. When the coefficients B_x, C_x, E_x are held constant, and $D_x = \mu_x F_z$, the longitudinal force is proportional to F_z and nonlinearly dependent on the slip.

In the case of the lateral force F_y , there are essentially two formulae depending on its intended use; for car, truck, or motorcycle tyres. In the case of car tyres, the formula resembles (3.91) and becomes

$$F_y = D_y \sin(C_y \arctan(B_y \tan \alpha - E_y(B_y \tan \alpha - \arctan(B_y \tan \alpha)))), \quad (3.93)$$

in which $\tan \alpha$ replaces κ . In the case of motorcycle tyres

$$F_y = D_y \sin(C_y \arctan(B_y \tan \alpha - E_y(B_y \tan \alpha - \arctan(B_y \tan \alpha))) + C_\gamma \arctan(B_\gamma \gamma - E_\gamma(B_\gamma \gamma - \arctan(B_\gamma \gamma)))), \quad (3.94)$$

where the effect of camber γ is explicitly accommodated; $C_y + C_\gamma < 2$ to prevent the side force from becoming negative at large slip and large camber angles. In the car version of the formula (3.93), the influence of camber is accounted for with a camber-dependent vertical shift. This approach is only appropriate when the camber force is small and thus cannot be used for motorcycle tyres. The cornering stiffness is $C_\alpha^{F_y} = B_y C_y D_y$ (recall (3.47)), while the camber stiffness is $C_\gamma^{F_y} = B_\gamma C_\gamma D_\gamma$ (recall footnote 7 and (3.67)).

In the case of F_y horizontal and vertical shifts can be used. For example, one may wish to recognize asymmetries in the tyre's construction that produce ply-steer, or pseudo-side-slip, which require a horizontal shift in the lateral slip plus a vertical shift in the force. Conicity, or pseudo-camber, can be accounted for with an horizontal shift in the camber and a vertical shift in the force.

While the magic formula parameters are typically load dependent, there are three whose load dependence is particularly important: the cornering stiffness $B_y C_y D_y$, the lateral peak force D_y , and the longitudinal peak force D_x . When considering these effects, the forces become nonlinearly dependent on the load. The cornering stiffness usually has a maximum, p_1 , at a certain load, $F_z = p_2$, and is thus modelled as

$$B_y C_y D_y = p_1 \sin(2 \arctan(F_z/p_2)). \quad (3.95)$$

This effect has significant implications for vehicle handling, including its over- or under-steering behaviour; see Section 4.2.1.

The friction coefficients usually decrease as the load increases, which translates into the nonlinear load dependency of the peak force factors D_x and D_y , which are modelled as:

$$D_y = \mu_y F_z = (p_{y3} + p_{y4} df_z) F_z \quad (3.96)$$

$$D_x = \mu_x F_z = (p_{x3} + p_{x4} df_z) F_z \quad (3.97)$$

in which $p_{y4} < 0$ and $p_{x4} < 0$ and $df_z = (F_z - F_{z0})/F_{z0}$ where F_{z0} is some reference load. This effect has implications for load transfer effects; see Section 7.2.3.

The formulae used for longitudinal and lateral force can also be used for the lateral-slip-related aligning moment. However, a slightly modified formula, the ‘cos-magic formula’, is usually preferred for the pneumatic trail that is used to generate the aligning moment:

$$t = D_t \cos(C_t \arctan(B_t \tan \alpha - E_t(B_t \tan \alpha - \arctan B_t \tan \alpha))). \quad (3.98)$$

The aligning moment is then computed as $M'_z = -tF_y|_{\gamma=0}$, where $F_y|_{\gamma=0}$ is the lateral force related to the lateral slip $\tan \alpha$. The aligning moment stiffness is $C_\alpha^{M'_z} = D_t B_y C_y D_y$ (recall (3.48)). The reason the camber-related lateral force is not taken into account is because its associated misaligning moment is not generated by the resultant of the lateral force moving behind the centre of the contact patch. Indeed, the camber-related resultant force passes through the centre of the contact patch to the limit of sliding, and then moves in front of it under sliding; see Section 3.4.3 and particularly Figure 3.8. As a final remark, the right-hand side of (3.98) is sometimes multiplied by $\cos \alpha = V_{Cx}/V_C$ to handle properly the case of large slip angles (where $t \approx 0$, and thus $M'_z \approx 0$) and possibly also reverse running (when t changes sign).

The misaligning component of M_z , which is mainly related to the camber and conicity, is called the residual torque M_z^r and is fitted with the formula

$$M_z^r = D_r \cos(\arctan B_r \tan \alpha), \quad (3.99)$$

where D_r is the peak value, which is attained when the lateral slip $\tan \alpha$ is zero. The term D_r contains the effect of camber, which is the dominant cause of misaligning moment (as shown in Section 3.4.3), since:

$$D_r = F_z(q_{r1}\gamma + q_{r2}|\gamma|). \quad (3.100)$$

The misaligning moment stiffness is $C_\gamma^{M_z^r} = F_z q_{r1}$ (recall footnote 7 and (3.68)). The whole moment results from the aligning moment and the residual moment:

$$M_z = M'_z + M_z^r. \quad (3.101)$$

The rolling resistance (not considered in the brush model in Section 3.4) is usually modelled as:

$$M_y = f_s F_z \quad (3.102)$$

$$f_s = (q_{s1} + q_{s2} V_r + q_{s3} V_r^4) r_0, \quad (3.103)$$

in which f_s is the rolling resistance coefficient, q_{s1} governs the initial (low speed) resistance, q_{s2} provides a small speed-related increase, and q_{s3} provides a further sharp

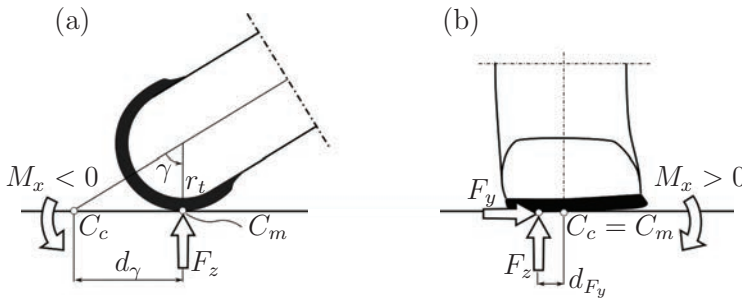


Figure 3.11: Overturning moment M_x and definitions of possible tyre-force points of application C . (a): the contribution related to camber γ is $M_x^{C_c} = -F_z d_\gamma$ (with $d_\gamma = r_t \tan \gamma$) and $M_x^{C_m} = 0$. (b): the contribution related to lateral force is $M_x^{C_c} = M_x^{C_m} = F_z d_{F_y}$ (shown positive in the figure, but negative values are possible).

rise in the rolling resistance that occurs when the critical velocity of the tyre is exceeded (standing waves produce large deformation and energy loss that eventually lead to tyre failure). The rolling resistance is caused by the effective point of application of F_z moving to the front half of the contact patch (due to hysteresis of the tread rubber).

The last of the three moment components is the overturning moment M_x . It is clear that this moment will depend on, amongst other things, the application point of the tyre-force system; see C in Figure 3.11. In car tyres it is common to use $C = C_c$, which is on the line of intersection between the wheel plane with the road surface. With motorcycle tyres it is more usual to define $C = C_m$, which is at the centre of the contact patch, as in the brush model described in Section 3.4.

In the case that C_c is used, the overturning moment has a camber-related contribution and a contribution related to the tyre lateral force F_y . The camber-related contribution is negative for $\gamma > 0$, because the force application point moves in the inclination direction (see Figure 3.11 (a)). Intuition might suggest that a positive lateral force $F_y > 0$ results in a negative moment (F_z moves in the direction of the lateral force), as a result of carcass lateral distortion. This is, however, not always the case, because an asymmetric distribution of the vertical loading may occur, resulting in a positive moment (F_z moves in a direction opposite to the F_y direction) (see Figure 3.11 (b)).¹²

When the C_m convention is used, the overturning moment derives from the lateral force alone, because the camber-related contribution is automatically included by geometry. This convention is particularly convenient for motorcycle tyres, where M_x is camber dominated. Another advantage of the convention will become apparent when dealing with coupling conditions, and in particular with the M_z arising from F_x when camber is present; see the discussion following (3.113).

¹² This phenomenon has been observed in car/truck tyres at low vertical loads, with a possible sign reversal (from $M_x > 0$ to $M_x < 0$) when some vertical load is exceeded [8].

In sum, in the case that the tyre forces are applied in C_c , the moment is modelled as:

$$M_x^{C_c} = \left(q_{x1} - q_{x2}\gamma + q_{x3}\frac{F_y}{F_z} \right) F_z, \quad (3.104)$$

while in the case that the forces system is applied at C_m the moment is:

$$M_x^{C_m} = \left(q_{x1} + q_{x3}\frac{F_y}{F_z} \right) F_z. \quad (3.105)$$

In these equations q_{x1} is an offset term, which can often be neglected; $q_{x2} > 0$ is a factor related to camber, with $d_\gamma = q_{x2}\gamma r_0$, producing a good fit to experimental data for small γ ; q_{x3} is related to the effect of lateral force, with $d_{F_y} = q_{x3}r_0 F_y/F_z$, which can be either positive or negative.¹³

The normal load is usually modelled as

$$F_z = p_z \max(\delta r, 0) (1 + p_{z2}|\Omega|) \quad (3.106)$$

where p_z is the static vertical stiffness of the tyre. The p_{z2} term governs the tyre growth resulting from the centrifugal force acting on the belt (which leads to an increase in the tyre radius with speed).

3.5.2 Combined slip

Equation (3.84) showed that the generation of F_x is compromised by the simultaneous generation of F_y and vice versa. In the magic formula world, cosinusoidal weighting functions G are used to represent this combined-force compromise. These weights reflect the effects of $\tan \alpha$ on F_x and κ on F_y as follows:

$$G_{x\alpha} = \cos(C_{x\alpha} \arctan(B_{x\alpha} \tan \alpha)) \quad (3.107)$$

$$G_{y\kappa} = \cos(C_{y\kappa} \arctan(B_{y\kappa} \kappa)), \quad (3.108)$$

where the B s influence the shape of G , while the C s are related to the function's support. The combined-slip forces are:

$$F_{xc} = F_x G_{x\alpha} \quad (3.109)$$

$$F_{yc} = F_y G_{y\kappa} \quad (3.110)$$

while the moment is:

$$M_{zc} = M'_z(\sigma_y^{eq}) + M_z^r(\sigma_y^{eq}) + s(\gamma, F_z)F_x. \quad (3.111)$$

The effective lateral slip is given by σ_y^{eq} and accounts for combined-slip influences and thus depends on κ , while s is the lever arm for the longitudinal force:

¹³ When C_m is a force application point that recognizes the lateral deformation of the carcass, (3.105) only has the q_{x1} term, which can usually be neglected and so $M_x = 0$ in this case.

$$\sigma_y^{eq} = \sqrt{(\tan \alpha)^2 + \left(\frac{B_x C_x D_x}{B_y C_y D_y} \right)^2} \kappa^2 \operatorname{sgn}(\alpha) \quad (3.112)$$

$$s = \left(s_{z1} + s_{z2} \frac{F_y}{F_{z0}} + s_{z3} \gamma \right). \quad (3.113)$$

It is worth noting that when employing the C_m convention (see Figure 3.11), $s_{z3} = 0$, because the camber-related component is automatically included in the setup geometry.¹⁴ A shift $\kappa \rightarrow \kappa + S_{Hy\kappa}$ may be introduced in (3.108) to account for the (small) increase in lateral force F_y experienced at moderate braking before the peak in $G_{y\kappa}$ is reached and F_y begins to decay (this effect is explained at the end of Section 3.4.4). If this shift is used, (3.108) must be divided by $\cos(C_{y\kappa} \arctan B_{y\kappa} S_{Hy\kappa})$ to ensure that $G_{y\kappa}(0) = 1$. In the same way, a κ -dependent vertical shift $S_{V_{y\kappa}}$ can be introduced in (3.110), which recognizes any κ -induced ply-steer; the apparent lateral slip associated with longitudinal-force induces deformation of the tread. Note that F_z and M_y are not affected by combined-slip effects.

Combined-slip effects can also be modelled using a more physical approach using concepts derived from the brush model in Section 3.4.4. The advantage of this approach is the retention of physical ideas and the further use of the pure slip curves—the empirical-coupling G functions are not required (or the combined slip measurement data used to parametrize them). The drawback is that the fit to experimental data is not as good as that achieved with the empirical approach.

The tyre forces are computed from the theoretical slips introduced above (the practical slips κ and $\tan \alpha$ can also be used), with the camber transformed into an equivalent slip angle:

$$\sigma_x = \frac{\kappa}{1 + \kappa} \quad \sigma_y = \frac{\tan \alpha^*}{1 + \kappa} \quad \sigma = \sqrt{\sigma_x^2 + \sigma_y^2} \quad (3.114)$$

where

$$\alpha^* = \alpha + \frac{B_\gamma C_\gamma D_\gamma}{B_y C_y D_y} \gamma. \quad (3.115)$$

The forces are now computed as:

$$F_{xc} = \frac{\sigma_x}{\sigma} F_x(\sigma) \quad (3.116)$$

$$F_{yc} = \frac{\sigma_y}{\sigma} F_y(\sigma). \quad (3.117)$$

In the same way the moment is:

$$M_z = \frac{\sigma_y}{\sigma} M'_z(\sigma) + q_{r1} F_z \gamma, \quad (3.118)$$

in which the first term is the aligning moment and the second term the residual moment (related to camber). The residual moment is sometimes multiplied by a factor that

¹⁴ When C_m recognizes the lateral deformation of the carcass, (3.113) only has the s_{z1} term, which can often be neglected and so $s(\gamma, F_x) = 0$.

makes the moment zero at large slip angles, say $1/(1+100\alpha^2)$. When comparing (3.118) with (3.111) it is clear that the F_x term is missing, since it is assumed that γ is small, and thus that this term is negligible, or the C_m convention is used (see Figure 3.11). Note that (3.116), (3.117), and (3.118) require no additional empirical coefficients.

In summary, the physical coupling approach requires: the pure longitudinal force curve (F_x vs. κ); the pure lateral force curve (F_y vs. $\tan \alpha$); the pneumatic trail curve (t vs. $\tan \alpha$); the lateral force camber stiffness ($\partial F_y / \partial \gamma = B_\gamma C_\gamma D_\gamma$); and the yawing moment camber stiffness ($\partial M_z^r / \partial \gamma = q_{r1} F_z$).

3.6 Behaviour in non-reference conditions

The characterization of tyre properties in terms of forces and torques, as functions of slip, is now a standardized procedure amongst car, motorcycle, and tyre manufacturers. It is again worth remembering that these measurements do not provide ‘absolute’ tyre properties, but the response of the tyre under specific test conditions (normal load, inflation pressure, test surface, and temperature).

For this reason it is useful to introduce a number of scaling factors in the magic formulae that were obtained under reference test conditions in order to predict (qualitatively) tyre behaviour under different (non-test) conditions. The idea is to exploit the fact that the pure slip curves remain broadly similar in shape when the tyre runs under conditions that are different from the reference conditions. Typical test conditions include the tyre’s rated (nominal) load (F_{z0}), rated inflation pressure (p_0), given road surface (μ_0), and temperature (T_p). These ideas build on the normalization theory of [90] as introduced in [108, 109]. Alternatively, the scaling factors of a specific tyre can be identified by testing under non-reference conditions [110].

3.6.1 Effect of normal load

A particular instance of a ‘variable parameter’ relates to changes in the normal load away from reference test conditions F_{z0} . The magic formulae can be extended to include changes in various coefficients through the normalized change in vertical load df_z

$$df_z = \frac{F_z - F_{z0}}{F_{z0}}. \quad (3.119)$$

These changes are usually accommodated as either linear or quadratic variations of the form [8]

$$A = A_0 + A_1 df_z + A_2 df_z^2 \quad (3.120)$$

in which A_0 is the reference value of A , and A_1 and A_2 represent linear and quadratic variations respectively in df_z .

The qualitative effect of an increase in normal load is as follows: an increase in the size of the contact patch, an increase in rolling resistance, an increase in the yawing moment, a change in the cornering stiffness (that depends on normal load and the tyre characteristics; see (3.95)). As already pointed out in (3.96)–(3.97), there is usually a reduction in the maximum achievable tyre friction as a consequence of an increase in

the normal load. A large contact patch is beneficial on dry surfaces, while a small one can be beneficial in wet conditions; see Section 3.6.4.

Basic tyre models include only a linear dependence of tyre force and moment on the normal load F_z . This is achieved by keeping constant the following coefficients introduced in Section 3.5: $B_{x,y,\gamma}$, $C_{x,y,\gamma}$, $E_{x,y,\gamma}$, $\mu_{x,y}$, D_t , q_{r1} , q_{r2} . Note that this results in constant slip stiffnesses per unit load: $C_{\kappa}^{F_x}/F_z = B_x C_x \mu_x$, $C_{\alpha}^{F_y}/F_z = B_y C_y \mu_y$, $C_{\gamma}^{F_y}/F_z = B_{\gamma} C_{\gamma} \mu_y$, $C_{\alpha}^{M_z}/F_z = D_t B_y C_y \mu_y$, $C_{\gamma}^{M_z}/F_z = q_{r1}$.

Good results are normally obtained when the variations of $C_{\alpha}^{F_y}/F_z$ and $\mu_{x,y}$ only depend on the normal load. This results in a nonlinear dependence of the tyre force and moment on F_z .

3.6.2 Effect of inflation pressure

The effect of pressure and pressure variations is a recent development of the magic formulae [104]. The changes are treated in much the same way as the changes in the normal load with a normalized change dp_i :

$$dp_i = \frac{p_i - p_0}{p_0}, \quad (3.121)$$

where p_0 is the reference inflation pressure.

The qualitative effect of an increase in inflation pressure is as follows: a reduction in the size of the contact patch, a reduction of rolling resistance, a reduction in the yawing moment, a change in the cornering stiffness that depends on the normal load and tyre characteristics [104, 111, 112]. These effects are usually neglected in simple models.

3.6.3 Effect of road surface

Tyre models are really tyre–road interaction models that can be significantly affected by changes in the road conditions. There are, however, some general trends that hold good [113, 114]. For example, when moving to wet (non hydroplaning) conditions, the friction peak is reduced, but there are generally only small changes in the cornering stiffness. In the same way, operation on different road surfaces may produce changes in the friction peak coefficient, but the cornering stiffness remains virtually unchanged. More generally, provided the road surface is ‘rigid’ relative to the tyre carcass, the cornering stiffness remains essentially the same (as predicted by the theoretical brush model).¹⁵ However, when considering off-road surfaces such as gravel, a reduction in the cornering stiffness is to be expected [115, 116]. In these cases the peak in the lateral force characteristic moves towards higher slips and may even disappear completely. On very soft surfaces a bulldozing effect akin to ‘ploughing’ may occur [117]. Similar changes to the longitudinal force characteristics may also be expected [116].

¹⁵ Note that changing the friction coefficients $\mu_{x,y}$ only, results in a unwanted change in the slip stiffnesses, unless one correspondingly changes $B_{x,y,\gamma}$ in order to keep the factor $B_{x,y,\gamma} C_{x,y,\gamma} \mu_{x,y}$ constant.

As common sense would suggest, different road conditions are likely to call for changes in driving strategy [118, 119]. For example, on a wet or poor road surface, one would expect to brake earlier on the entrance to corners, accelerate more gently on the exit from corners, and possibly modify the line taken through bends [120].

3.6.4 Hydroplaning

Hydroplaning or *aquaplaning* is the partial or total lost of contact between the tyre and the road as a consequence of the hydrodynamic pressure generated by the tyre rolling over a layer of water [121]; this phenomenon is usually associated with driving/riding through puddled water at elevated speeds. In the case of partial hydroplaning, the effect is localized around the leading edge of the contact patch. In extreme cases one experiences a sustained loss of traction and the vehicle becomes non-responsive to steering inputs. For motorcycles, hydroplaning is particularly serious, because the vehicle becomes unstable as well as uncontrollable when the tyre force system is compromised.

The phenomenon was first observed in the late 1950s, whilst its basics were reported in the early 1960s [122], together with a simple formula for the prediction of the hydroplaning critical speed. Under hydroplaning conditions the mean pressure on the contact patch F_z/A is equal to the mean hydrodynamic pressure p_h given by

$$p_h = \frac{1}{2} \rho C_L (V_C^h)^2 \quad \Rightarrow \quad V_C^h = \sqrt{\frac{2}{\rho C_L} \frac{F_z}{A}} = \sqrt{\frac{p_h}{K}}, \quad (3.122)$$

where ρ is the water density, $A = 4ab$ is the area of the contact patch, V_C^h is the tyre hydroplaning critical speed, and $K = 322$ in the original study, where it was further assumed that the inflation pressure was the mean pressure over the contact patch.¹⁶ Equation (3.122) gives critical speeds of 25 m/s (90 km/h), and 50 m/s with inflation pressures of 2 bar (typical of car tyres) and 8 bar (typical of truck tyres) respectively, and is still in use to determine the hydroplaning potential of road surfaces [123]. When the vehicle speed exceeds the critical hydroplaning speed given by (3.122) by more than 8 km/h, and the water film thickness exceeds 1.5 mm, the hydroplaning risk is deemed to be ‘high’. If the water film thickness is less than 0.5 mm, conditions are deemed to be safe from a hydroplaning perspective [123]. Depending on the tread pattern, and the shape and size of the contact patch, K varies over the range 250 (high-performance grooved tyres) to 500 (slick tyre).

The road macro-texture and tyre tread depth influence the onset of dynamic hydroplaning in two ways. First, they have a direct effect on the critical hydroplaning speed, because they provide a pathway for water to escape from the road–tyre interface. Second, they have an indirect effect on the critical hydroplaning speed, since the larger the macro-texture, the deeper the water must be to cause hydroplaning. However, the road surface must also have the proper micro-texture to develop adequate friction.

¹⁶ The two pressures would indeed be exactly the same if the carcass bending stiffness was zero (membrane assumption). In practice the inflation pressure is somewhat lower (e.g. 2 bars vs 3 bars).

Another factor influencing hydroplaning potential is the shape of the contact patch. Rounded contact patches (motorcycle tyres) result in higher critical speeds as compared with rectangular contact patches (car tyres). If β is the angle between the normal to the leading edge and the direction of travel, the velocity component contributing to the dynamic pressure is $V \cos \beta$; aircraft wings are swept back for the same reason. Detailed numerical analyses of the tyre hydroplaning behaviour based on coupled CFD (computational fluid dynamics) and FEM (finite element method) were reported in the late 1990s [124].

3.6.5 Thermal effects

While temperature has a significant effect on tyre behaviour, thermal influences are not currently included in magic formula tyre models. The effect of temperature is particularly important in the racing context, where high-performance tyre compounds provide maximal tyre–road friction over a limited range of temperatures [125]. Variations in the track surface roughness and the ambient temperature have led tyre manufacturers to develop a range of compounds, each with its own friction and durability characteristics.

The relationships between friction generation and the compound's viscoelastic properties have been examined by several authors [126–128]. These studies are based on the seminal work of Grosch [129], who demonstrated that the adhesive and hysteretic components of friction can be characterized by a spacial-frequency-dependent master curve. The frequency–temperature equivalence described in [130] uses a scaling factor to correct these master curves for temperature variations.

Friction is an energy-dissipation mechanism that results in surface degradation and wear. With this in mind, Moore [131] examines the relationship between friction, fatigue, abrasion, and wear mechanisms for road car tyre rubber compounds. In the case of slick racing tyres, in combination with a rough, dry track, high friction coefficients and abrasive wear and *graining* are dominant phenomena [132]. A qualitative assessment of these processes is made in [133], which highlights the importance of the frequency of road asperities. The large body of experimental work, which is summarized in [134–136], shows that temperature, slip velocity, normal load, and the topology of abrasive surfaces are all key friction-influencing features.

Figure 3.12 shows how the tyre friction coefficient might vary with tyre tread temperature; the friction factor λ_μ is the ratio between the friction at the optimal reference temperature and the friction available at other temperatures T_p . Peak friction is achieved between the temperatures T_{p1} and T_{p2} ; one might expect the midpoint between T_{p1} and T_{p2} to be of the order 100°C with $\lambda_\mu > 0.95$ over the tyre's operating temperature range. The longitudinal and lateral tyre forces, as modelled by magic formulae, are scaled by λ_μ ; these details are often commercially sensitive.

In order to exploit tyre thermal sensitivities in simulation, or optimal control studies, it is necessary to track the tyre tread temperature variations. This can be done using a simple lumped-parameter model that describes the heat flows into the tread mass; high-frequency temperature variations associated with the rotation of the wheels are not considered. The dominant heat flows considered in the analysis are shown schematically in Figure 3.13 and consist of the following:

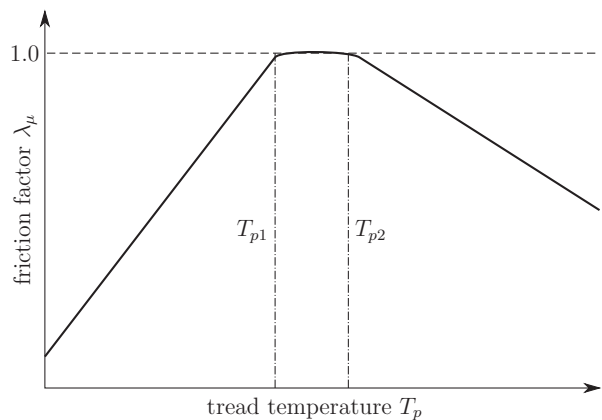


Figure 3.12: Friction factor λ_μ against the tyre tread temperature T_p .

- (a) Q_1 —heat generation in the sliding region of the contact patch
- (b) Q_2 —heat generation due to tyre carcass deflection
- (c) Q_3 —convective cooling through ambient air surrounding tyre
- (d) Q_4 —conductive cooling in the non-sliding region of the contact patch

The tyre tread surface temperature T_p is described by:

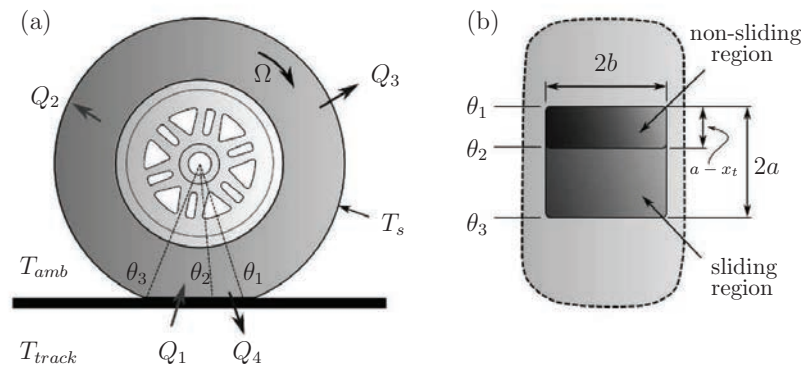


Figure 3.13: (a) Dominant heat flows that determine the tyre tread temperature T_p . The angle θ_1 defines the angle at which the leading edge of the contact patch is located. The angle θ_2 denotes the transition between the adhesion and the sliding regions, while θ_3 marks the end of the trailing edge. (b) View from the bottom of the tyre detailing the contact-patch geometry.

$$m_t c_t \frac{d}{dt} T_p = Q_1 + Q_2 - Q_3 - Q_4, \quad (3.123)$$

where c_t is the specific heat capacity of the tyre tread and m_t its mass. The heat generated from the sliding region of the contact patch is calculated through summation of longitudinal and lateral slip powers:

$$Q_1 = p_1 V_{Cx} (|F_x| \kappa + |F_y| \tan \alpha), \quad (3.124)$$

where the slip quantities α, κ , and the tyre forces F_x, F_y , are derived from the tyre model. The parameter p_1 accounts for the proportion of frictional power lost to the track in the sliding region of the contact patch. Heat generation due to bulk tyre deflection is treated in a manner similar to that described in [126], with the parameters p_2 through p_4 describing efficiency terms. These relate to the magnitude of heat generated as a result of longitudinal, lateral, and normal tyre forces

$$Q_2 = V_{Cx} (p_2 |F_x| + p_3 |F_y| + p_4 |F_z|). \quad (3.125)$$

The convective cooling of each tyre through the ambient air temperature T_{amb} is dealt with using the cooling law:

$$Q_3 = p_5 V_{Cx}^{p_6} (T_p - T_{amb}), \quad (3.126)$$

where the heat transfer coefficient $V_{Cx}^{p_6}$ is a nonlinear function of the vehicle speed [137] and parameters p_5 and p_6 are used to control the variations in airflow associated with each corner of the vehicle. The conductive cooling through the non-sliding region of the contact patch is determined by:

$$Q_4 = h_t A_{ns} (T_p - T_{track}), \quad (3.127)$$

where h_t is the heat transfer coefficient between the track and tyre, A_{ns} is the non-sliding area of the contact patch, and T_{track} the track temperature. The width of the contact patch $2b$ is assumed constant, with the length $2a$ defined by a fractional power β of the normal load:

$$2a = a_{cp} F_z^\beta. \quad (3.128)$$

The constant a_{cp} reflects contact-patch length deformation. Following the Brush model convention (see Section 3.4), the transition point between the sliding and non-sliding region is x_t and is given by

$$\frac{x_t}{2a} = \hat{\theta}_P |\sigma| - \frac{1}{2}, \quad (3.129)$$

where $\hat{\theta}_P$ is an estimate of θ_P ; see (3.83). The resulting non-sliding contact-patch area is calculated using:

$$A_{ns} = 2b (a - x_t). \quad (3.130)$$

The six parameters p_1 through p_6 can be determined using nonlinear least-squares fitting against measured data [125]. Figure 3.14 shows the measured and predicted temperature variations for a Formula One car on one lap of a closed-circuit track. Significant are the facts that the temperature profiles of the four tyres are significantly different and that the tyre tread surface temperature can vary by almost 100° C within a single lap of approximately 4.6 km.

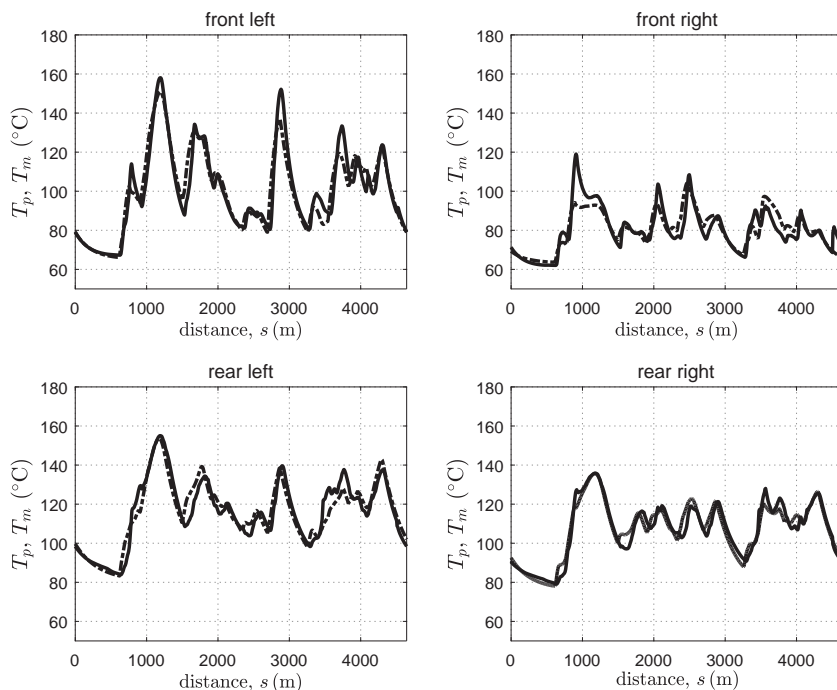


Figure 3.14: Tyre tread surface temperature measurements T_m (shown solid) and model values T_p (shown dot-dashed) [125].

3.7 Unsteady behaviour: string model

In this section the ‘string model’, first introduced in [138], is used to explain the essentials of transient tyre force generation. Later developments include [139] (derivation of frequency response), [92] (string with tread element), and [140] (computation of exact model response). More recently [87] compared several earlier models. In this development rolling resistance is neglected, complete adhesion is assumed, and all deformations are treated as small. As a consequence the resulting model is linear and holds only for small perturbations around straight-running trim conditions. The discussion is restricted to lateral motion (lateral slip α and spin slip φ_s) and the resulting lateral force F_y and moment M'_z (note that M'_z is used in place of $M_z = M'_z + M_z^r$, because the tyre is considered thin).

As shown in Figure 3.15, the tyre is treated as a loaded string in equilibrium. In the radial direction the string is held taut by a distributed radial force associated with the tyre’s inflation. In the axial direction the string is supported elastically relative to the wheel-centre plane; no circumferential freedom being allowed. The string contacts a smooth horizontal road over the length of the contact patch, but extends over the tyre’s perimeter. The string offers no resistance to bending, and so the only internal force is the tension F that acts in a direction tangent to the deflection curve. The

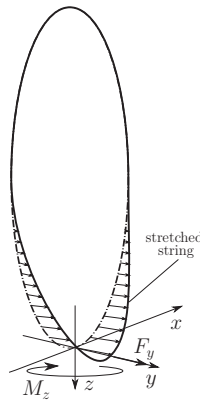


Figure 3.15: Tyre tread modelled as a stretched string.

ordinate of the deflection is given by $\bar{y}(x)$, in the $(Cxyz)$ coordinate system that moves with the wheel; see Figure 3.4. The angle between the x -axis and the tangent to the deflection curve is θ . The string load per unit length in the y -axis direction is $p(x)$. Figure 3.16 shows a plan view of the taut string, which has been deflected away from the wheel centre line by the lateral loading $p(x)$, which is given by

$$p(x) = \begin{cases} -K_{Py}\bar{y} & |x| > a \\ q_y - K_{Py}\bar{y} & |x| \leq a, \end{cases} \quad (3.131)$$

where q_y is the frictional shear force per unit length, K_{Py} is the tyre lateral stiffness per unit length (as in the brush model), and \bar{y} is the lateral deflection of the tread-base material. The equilibrium equations for an element between x and $x + dx$ are

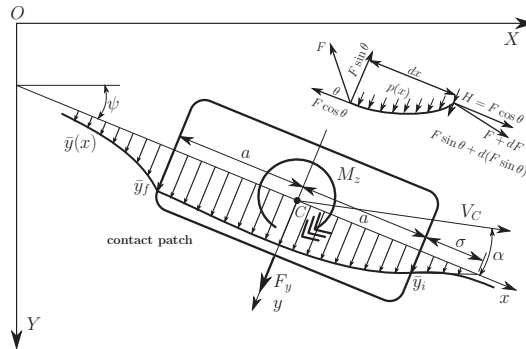


Figure 3.16: Plan view of the single-string model and its position with respect to the fixed reference frame. The insert shows the balance of forces on a string element of length dx .

$$\frac{d}{dx}(F \cos \theta) = 0 \quad (3.132)$$

$$\frac{d}{dx}(F \sin \theta) = -p(x). \quad (3.133)$$

Equation (3.132) shows that the horizontal component of the tension $H = F \cos \theta$ is constant. Eliminating F in (3.133) gives

$$H \frac{d}{dx}(\tan \theta) = -p(x), \quad (3.134)$$

or since $\tan \theta = d\bar{y}/dx$

$$H \frac{d^2 \bar{y}}{dx^2} = K_{Py} \bar{y} \quad (3.135)$$

from (3.131) when $|x| > a$ and

$$H \frac{d^2 \bar{y}}{dx^2} = K_{Py} \bar{y} - q_y \quad (3.136)$$

when $|x| \leq a$. The general form of the solution to (3.135) is easily checked to be

$$\bar{y} = c_i e^{-x/\sigma} + c_f e^{x/\sigma}, \quad (3.137)$$

where

$$\sigma = \sqrt{\frac{H}{K_{Py}}} \quad (3.138)$$

with c_i and c_f constants. The solution to (3.136) includes a particular integral

$$\bar{y} = c_i e^{-x/\sigma} + c_f e^{x/\sigma} + \frac{q_y}{K_{Py}}. \quad (3.139)$$

Referring to Figure 3.15, it is physically reasonable to suppose also that $\lim_{x \rightarrow \infty} \bar{y}(x) = 0$, and so

$$\bar{y} = c_i e^{-x/\sigma} \quad x > a. \quad (3.140)$$

Similarly

$$\bar{y} = c_f e^{x/\sigma} \quad (3.141)$$

when $x < -a$. This analysis assumes that the circumference of the tyre is much larger than the contact length. As a result the deflections for $x > a$ and $x < -a$ become independent of one another.

Since $\bar{y}(a) = \bar{y}_i$ at the leading edge of the contact patch and $\bar{y}(-a) = \bar{y}_f$ at the trailing edge, there hold

$$\bar{y} = \bar{y}_i e^{(a-x)/\sigma} \quad x > a \quad (3.142)$$

$$\bar{y} = \bar{y}_f e^{(a+x)/\sigma} \quad x < -a. \quad (3.143)$$

Although the string is assumed to have zero bending stiffness, the physics of the rolling process suggests that the gradient $d\bar{y}/dx$ is continuous in $x = a$ (this is not necessarily true at $x = -a$). Since $\frac{d\bar{y}}{dx}|_{x=a} = -\bar{y}_i/\sigma = \tan \theta_i$, σ can be interpreted as a ‘length’ as shown in Figure 3.16, and is called the *relaxation length*.

3.7.1 Side slip and spin slip

In Section 3.3 we derived differential equations describing the sliding velocities of a rolling wheel. In the case of lateral slip α , and spin slip φ_s , with zero sliding velocities, it follows from (3.25) that

$$\frac{\partial \bar{y}}{\partial x} = \frac{\partial \bar{y}}{\partial s} - \alpha - x\varphi_s. \quad (3.144)$$

We remind the reader that in this equation s denotes the distance travelled by the centre of the contact patch. The variables x and y denote the location of an arbitrary stressed material point with respect to the moving axes system $Cxyz$. This partial differential equation introduces ‘dynamics’ into the tyre model and will be solved using Laplace transforms; the travelled distance s (rather than time) is the independent variable in this case. The Laplace variable is denoted p and transformed variables are preceded by \mathcal{L} . The equation is now converted into an ordinary linear differential equation (in the independent variable x):

$$\frac{\partial \mathcal{L}\bar{y}}{\partial x} - p\mathcal{L}\bar{y} = -\mathcal{L}\alpha - x\mathcal{L}\varphi_s \rightarrow \mathcal{L}\bar{y} = c_{\bar{y}}e^{px} + \frac{1}{p} \left(\mathcal{L}\alpha + \left(\frac{1}{p} + x \right) \mathcal{L}\varphi_s \right). \quad (3.145)$$

The constant $c_{\bar{y}}$ is obtained from the boundary condition on the leading edge of the contact patch:

$$\left. \frac{\partial \mathcal{L}\bar{y}}{\partial x} \right|_{x=a} = -\frac{\mathcal{L}\bar{y}_i}{\sigma} \rightarrow c_{\bar{y}} = -\frac{e^{-pa}}{p} \left(\frac{\mathcal{L}\bar{y}_i}{\sigma} + \frac{\mathcal{L}\varphi_s}{p} \right). \quad (3.146)$$

Substituting (3.146) into (3.145) gives

$$\mathcal{L}\bar{y} = \frac{1}{p} \left(-\frac{\mathcal{L}\alpha + \left(\sigma + a + \frac{1}{p} \right) \mathcal{L}\varphi_s}{\sigma p + 1} e^{p(x-a)} + \mathcal{L}\alpha + \left(x + \frac{1}{p} \right) \mathcal{L}\varphi_s \right). \quad (3.147)$$

The force F_y and the moment M'_z exerted on the tyre will now be computed with the aid of Figure 3.17. Summing forces in the y -axis direction gives

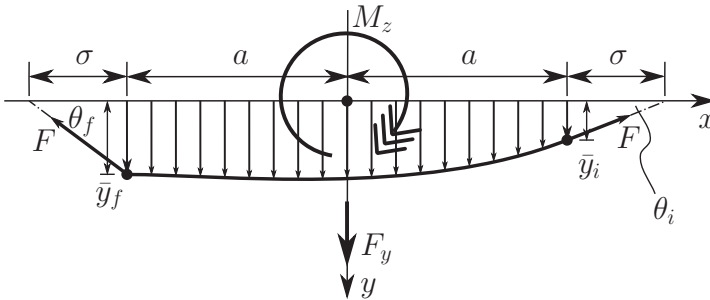


Figure 3.17: Free-body diagram of the taught string.

$$\begin{aligned}
F_y &= K_{Py} \int_{-a}^{+a} \bar{y} dx + F(\sin \theta_f + \sin \theta_i) = K_{Py} \int_{-a}^{+a} \bar{y} dx + H(\tan \theta_f + \tan \theta_i) \\
&= K_{Py} \int_{-a}^{+a} \bar{y} dx + H \left(\frac{\bar{y}_i + \bar{y}_f}{\sigma} \right); \tag{3.148}
\end{aligned}$$

the lateral tyre force has to oppose the string tension and distort the tread base material. Taking moments around the origin in Figure 3.17 gives

$$\begin{aligned}
M'_z &= K_{Py} \int_{-a}^{+a} \bar{y} x dx + H(a \tan \theta_i + \bar{y}_i) - H(a \tan \theta_f + \bar{y}_f) \\
&= K_{Py} \int_{-a}^{+a} \bar{y} x dx + H(\bar{y}_i - \bar{y}_f) \left(\frac{a + \sigma}{\sigma} \right). \tag{3.149}
\end{aligned}$$

It is now possible to find transfer functions between α and φ_s , and F_y and M'_z , using Laplace-transformed versions of (3.148) and (3.149). To do this we will require (3.138), which is used to eliminate H , and (3.147), which is used to compute \bar{y}_i , \bar{y}_f , and \bar{y} . A direct, but tedious computation gives:

$$\mathbf{G}_{\alpha}^{F_y} = \frac{K_{Py}}{p} \left[2(\sigma + a) - \frac{1}{p} \left(1 + \frac{\sigma p - 1}{\sigma p + 1} e^{-2pa} \right) \right] \tag{3.150}$$

$$\mathbf{G}_{\varphi_s}^{F_y} = \frac{K_{Py}}{p^2} \left[2(\sigma + a) - \frac{1}{p} \left(1 + \frac{\sigma p - 1}{\sigma p + 1} e^{-2pa} \right) (p(\sigma + a) + 1) \right] \tag{3.151}$$

$$\mathbf{G}_{\alpha}^{M'_z} = -\mathbf{G}_{\varphi_s}^{F_y} \tag{3.152}$$

$$\begin{aligned}
\mathbf{G}_{\varphi_s}^{M'_z} &= \frac{K_{Py}}{p} \left[2a \left(\sigma(\sigma + a) + \frac{a^2}{3} \right) - \frac{1}{p} \left((\sigma + a)^2 - \frac{1}{p^2} \right) \right. \\
&\quad \left. + \frac{1}{p} \left(\sigma + a + \frac{1}{p} \right)^2 \frac{\sigma p - 1}{\sigma p + 1} e^{-2pa} \right], \tag{3.153}
\end{aligned}$$

where $\mathbf{G}_{\alpha}^{F_y}$ is the transfer function mapping α to F_y and so on. As with the brush model, reciprocity between $\mathbf{G}_{\alpha}^{M'_z}$ and $\mathbf{G}_{\varphi_s}^{F_y}$ is found. As a result of linearity, the full lateral force and aligning moment responses come from superimposing (3.150) and (3.151), and (3.152) and (3.153) respectively.

In the context of the brush model, the cornering stiffness, the aligning moment stiffness, the spin-slip force stiffness, and the spin-slip moment stiffness were computed by considering limits in which $\alpha \rightarrow 0$ and $\varphi_s \rightarrow 0$. We can recover these relationships from (3.150), (3.151), (3.152), and (3.153) by invoking the final-value theorem associated with the Laplace transform. Formally

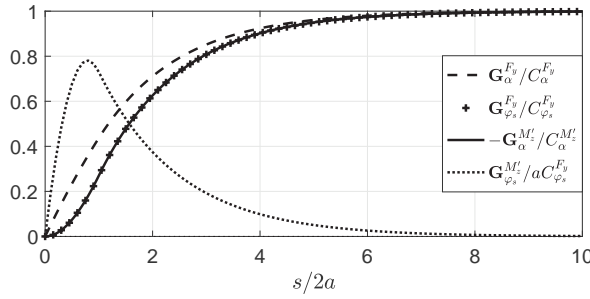


Figure 3.18: Normalized step responses for the transfer functions given in (3.150)–(3.153); $s/2a$ is the elapsed distance normalized to the length of the contact patch and $\sigma = 3a$.

$$C_{\alpha}^{F_y} = \lim_{p \rightarrow 0} \mathbf{G}_{\alpha}^{F_y} = 2K_{Py}(\sigma + a)^2 \quad (3.154)$$

$$C_{\phi_s}^{F_y} = \lim_{p \rightarrow 0} \mathbf{G}_{\phi_s}^{F_y} = 2K_{Py}a \left(\sigma(\sigma + a) + \frac{a^2}{3} \right) \quad (3.155)$$

$$C_{\alpha}^{M'_z} = \lim_{p \rightarrow 0} -\mathbf{G}_{\alpha}^{M'_z} = C_{\phi_s}^{F_y} \quad (3.156)$$

$$C_{\phi_s}^{M'_z} = \lim_{p \rightarrow 0} \mathbf{G}_{\phi_s}^{M'_z} = 0 \quad (3.157)$$

with the pneumatic trail given by

$$t = \frac{C_{\alpha}^{M'_z}}{C_{\alpha}^{F_y}} = \frac{a \left(\sigma(\sigma + a) + \frac{a^2}{3} \right)}{(\sigma + a)^2}. \quad (3.158)$$

The brush-model slip stiffnesses in (3.47), (3.48), (3.67), and (3.68), and the pneumatic trail in (3.49), are recovered when $\sigma = 0$ is substituted into (3.154)–(3.158). By referring to (3.138), we see that $\sigma = 0$ corresponds to the removal of the string tension.

The (normalized) step responses for the four transfer functions (3.150)–(3.153) are given in Figure 3.18. As is self-evident, each response comprises the sum of a rational response term and a delayed term, the delay being associated with the time of travel through the contact patch.

When the low-frequency/large-wavelength behaviour is of interest, the delay terms in (3.150)–(3.153) can be approximated by truncated power series expansions around $p = 0$.¹⁷ From (3.150) one obtains

$$\begin{aligned} (\sigma p + 1)\mathbf{G}_{\alpha}^{F_y} &= K_{Py} \left(2p^2\sigma(a + \sigma) + p(2a + \sigma) - 1 + e^{-2ap}(1 - \sigma p) \right) / p^2 \\ &= C_{\alpha}^{F_y} (1 - (a - t)p) + O(p^2), \end{aligned} \quad (3.159)$$

¹⁷ Specifically $\frac{e^{-2ap}}{p} = \frac{1}{p} - 2a + 2pa^2 + O(p^2)$ and $\frac{e^{-2ap}}{p^2} = \frac{1}{p^2} - \frac{2a}{p} + 2a^2 - \frac{4}{3}a^2p + O(p^2)$.

which is equivalent to the following first-order linear differential equation description

$$\sigma \frac{dF_y}{ds} + F_y = C_{\alpha}^{F_y} (\alpha - (a - t) \frac{d\alpha}{ds}), \quad (3.160)$$

where the pneumatic trail t is given in (3.158). Similar (somewhat tedious) calculations give

$$\sigma \frac{dF_y}{ds} + F_y = C_{\varphi_s}^{F_y} (\varphi_s - a \frac{d\varphi_s}{ds}); \quad (3.161)$$

$$\sigma \frac{dM'_z}{ds} + M'_z = -C_{\alpha}^{M'_z} (\alpha - a \frac{d\alpha}{ds}); \quad (3.162)$$

$$\sigma \frac{dM'_z}{ds} + M'_z = a \left(\left(\sigma + \frac{a}{3} \right) C_{\alpha}^{M'_z} + \frac{a}{15} \left(C_{\alpha}^{M'_z} - \frac{a \sigma C_{\alpha}^{F_y}}{\sigma + a} \right) \right) \frac{d\varphi_s}{ds}. \quad (3.163)$$

Note that the whole lateral force results from the summation of the component related to the side slip (3.160) and the component related to the spin slip (3.161). Similarly, the whole yawing moment results from (3.162) and (3.163). Closely related alternative reduced-order tyre models can be found by exploiting the quasi-steady approximation $C_{\alpha}^{F_y} d\alpha/ds = dF_y/ds$, $C_{\varphi_s}^{F_y} d\varphi_s/ds = dF_y/ds$, and $C_{\alpha}^{M'_z} d\alpha/ds = dM'_z/ds$. Substituting the first of these relationships into (3.160), the second into (3.161), and the third into (3.162) gives

$$(\sigma + a - t) \frac{dF_y}{ds} + F_y = C_{\alpha}^{F_y} \alpha \quad (3.164)$$

$$(\sigma + a) \frac{dF_y}{ds} + F_y = C_{\varphi_s}^{F_y} \varphi_s \quad (3.165)$$

$$(\sigma + a) \frac{dM'_z}{ds} + M'_z = C_{\alpha}^{M'_z} \alpha. \quad (3.166)$$

Note that (3.163) has been left as is. The effect of these approximations can be seen in Figure 3.19. A notable practical difference between the exact model and the approximated model is that the step response of the former is exponential only after the tyre has travelled a distance $2a$ (when the last tread point that was making contact before the step took place leaves the contact patch). In contrast, the approximated model gives exponential responses. This suggests that the approximated model is acceptable when the path frequencies are such that the related wavelengths are much larger than the contact length, which is the case for most handling manoeuvres and low-frequency instabilities. At higher frequencies more elaborate models may be required.

In addition to its physical relationship with the slope of the contact line as shown in Figure 3.17, the relaxation length σ has a dynamic meaning relating to the temporal development of tyre forces and moments. The longer the relaxation length, the slower the dynamic response of the tyre force/moment to changes in the inputs α and/or φ_s ; since σ is a spatial constant, and $ds = V_{Cx} dt$, σ/V_{Cx} is a time constant. In other words, when using the model in (3.160)–(3.163), σ is the distance travelled and σ/V_{Cx} is the time taken for the tyre to generate $\sim 63\%$ of its steady-state force/moment

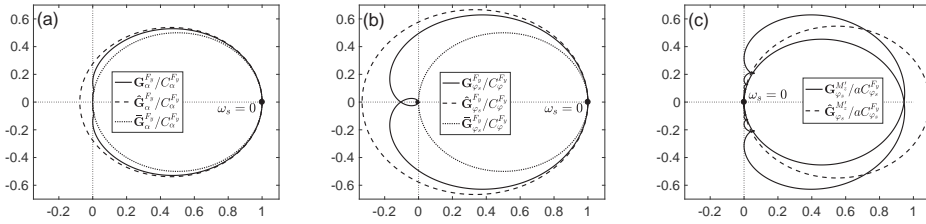


Figure 3.19: (a) shows normalized Nyquist diagrams of $\mathbf{G}_\alpha^{F_y}$ given in (3.150), the rational approximation $\hat{\mathbf{G}}_\alpha^{F_y}$ given in (3.160), and the rational approximation $\bar{\mathbf{G}}_\alpha^{F_y}$ given in (3.164). (b) shows normalized Nyquist diagrams of $\mathbf{G}_{\varphi_s}^{F_y}$ given in (3.151), the rational approximation $\hat{\mathbf{G}}_{\varphi_s}^{F_y}$ given in (3.161), and the rational approximation $\bar{\mathbf{G}}_{\varphi_s}^{F_y}$ given in (3.165). (c) shows normalized Nyquist diagrams of $\mathbf{G}_{\varphi_s}^{M'_z}$ given in (3.153) and the rational approximation $\hat{\mathbf{G}}_{\varphi_s}^{M'_z}$ given in (3.163); $\omega_s = 0$ represents zero spatial frequency.

after a step change in the (slip) input. When using (3.164)–(3.166) and (3.163), three different relaxation lengths are involved, namely $\sigma + a - t$, $\sigma + a$, and σ .

Various other approximate models have been developed over the years. We mention for example Von Schlippe's straight connection model, which assumes a straight contact line between the leading and trailing edges of the contact patch [138]; the straight tangent model, which assumes a straight contact line with the leading-edge gradient maintained across the contact patch; and the single-point contact model, which disregards the geometry of the contact patch. A comprehensive summary of this material can be found in [8].

3.7.2 Transfer function relationships

In this section we derive relationships between the transfer functions associated with the tyre slips α and φ_s , as well as those associated with the tyre lateral displacement y and orientation ψ . We will also show that the dynamic response of the string model reduces to its quasi-steady response when yaw oscillations take place around an axis located $\sigma + a$ ahead of the centre of the contact patch C .

In the case that $\gamma = 0$, and assuming $ds \approx V_{Cx}dt$, one obtains

$$\varphi_s = \varphi_t = -\frac{d\psi}{ds} \quad (3.167)$$

from (3.15) and so

$$\mathcal{L}\varphi_s = \mathcal{L}\varphi_t = -p\mathcal{L}\psi. \quad (3.168)$$

For a straight-running wheel subject to small yaw oscillations, $V_C \approx V_{Cx}$ and the wheel's lateral velocity is given by $V_{Cy} = V_{Sy} = \dot{y} - \psi V_{Cx}$. This gives

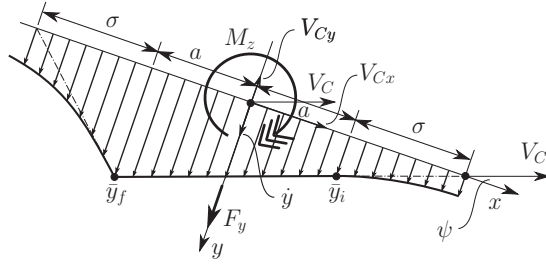


Figure 3.20: Wheel and tyre subject to small yaw oscillations around an axis located $\sigma + a$ ahead of the patch centre C .

$$\alpha = -\frac{V_{Sy}}{V_{Cx}} = \frac{V_{Cx}\psi - \dot{y}}{V_{Cx}} = \psi - \frac{1}{V_{Cx}} \frac{dy}{dt} = \psi - \frac{dy}{ds} \quad (3.169)$$

and so

$$\mathcal{L}\alpha = \mathcal{L}\psi - p\mathcal{L}y. \quad (3.170)$$

The relationships between the slip- and displacement-related transfer functions can now be found. From (3.168) and (3.170) there follows

$$\begin{aligned} \mathcal{L}F_y &= \mathbf{G}_{\alpha}^{F_y} \mathcal{L}\alpha + \mathbf{G}_{\varphi_s}^{F_y} \mathcal{L}\varphi_s \\ &= \mathbf{G}_{\alpha}^{F_y} (\mathcal{L}\psi - p\mathcal{L}y) + \mathbf{G}_{\varphi_s}^{F_y} (-p\mathcal{L}\psi) \\ &= \underbrace{(\mathbf{G}_{\alpha}^{F_y} - p\mathbf{G}_{\varphi_s}^{F_y})}_{\mathbf{G}_{\psi}^{F_y}} \mathcal{L}\psi + \underbrace{(-p\mathbf{G}_{\alpha}^{F_y})}_{\mathbf{G}_y^{F_y}} \mathcal{L}y. \end{aligned} \quad (3.171)$$

In the same way the moments are described by

$$\begin{aligned} \mathcal{L}M'_z &= \mathbf{G}_{\alpha}^{M'_z} \mathcal{L}\alpha + \mathbf{G}_{\varphi_s}^{M'_z} \mathcal{L}\varphi_s \\ &= \underbrace{(\mathbf{G}_{\alpha}^{M'_z} - p\mathbf{G}_{\varphi_s}^{M'_z})}_{\mathbf{G}_{\psi}^{M'_z}} \mathcal{L}\psi + \underbrace{(-p\mathbf{G}_{\alpha}^{M'_z})}_{\mathbf{G}_y^{M'_z}} \mathcal{L}y. \end{aligned} \quad (3.172)$$

It follows from (3.154) and (3.155), and (3.171) and (3.172), that

$$C_{\psi}^{F_y} = \lim_{p \rightarrow 0} \mathbf{G}_{\psi}^{F_y} = C_{\alpha}^{F_y}, \quad (3.173)$$

$$C_{\psi}^{M'_z} = \lim_{p \rightarrow 0} -\mathbf{G}_{\psi}^{M'_z} = C_{\alpha}^{M'_z}. \quad (3.174)$$

A further two relationships can be derived from an analysis of the response of the string model to the particular inputs contemplated in Figure 3.20. Since the lateral displacement of the contact patch centre is given by $\mathcal{L}y = -(a + \sigma)\mathcal{L}\psi$, there holds

$$\begin{aligned} \mathcal{L}F_y &= \mathbf{G}_{\psi}^{F_y} \mathcal{L}\psi + \mathbf{G}_y^{F_y} \mathcal{L}y \\ &= \mathbf{G}_{\psi}^{F_y} \mathcal{L}\psi - (a + \sigma)\mathbf{G}_y^{F_y} \mathcal{L}\psi \\ &= \left(\mathbf{G}_{\alpha}^{F_y} - p\mathbf{G}_{\varphi_s}^{F_y} + (a + \sigma)p\mathbf{G}_{\alpha}^{F_y} \right) \mathcal{L}\psi. \end{aligned} \quad (3.175)$$

Direct calculation using (3.150), (3.151), and (3.154) gives

$$\mathcal{L}F_y = C_\alpha^{F_y} \mathcal{L}\psi. \quad (3.176)$$

The same reasoning leads to an equivalent relationship for the moment

$$\mathcal{L}M'_z = C_\alpha^{M'_z} \mathcal{L}\psi. \quad (3.177)$$

Equations (3.176) and (3.177) give

$$C_\alpha^{F_y} = \mathbf{G}_\psi^{F_y} + p(a + \sigma)\mathbf{G}_\alpha^{F_y} \quad (3.178)$$

$$C_\alpha^{M'_z} = \mathbf{G}_\psi^{M'_z} + p(a + \sigma)\mathbf{G}_\alpha^{M'_z}. \quad (3.179)$$

While (3.178) and (3.179) have been suggested by the analysis associated with Figure 3.20, they are true in general.

Six constraints on $\mathbf{G}_{\alpha, \varphi_s, y, \psi}^{F_y}$ and $\mathbf{G}_{\alpha, \varphi_s, y, \psi}^{M'_z}$ are thus given by (3.171), (3.172), and (3.178) and (3.179). The utility of these results comes from the fact that any one of $\mathbf{G}_\alpha^{F_y}$, $\mathbf{G}_{\varphi_s}^{F_y}$, $\mathbf{G}_\psi^{F_y}$, and $\mathbf{G}_y^{F_y}$ determines the other three; the same applies to the moment relationships $\mathbf{G}_{\alpha, \varphi_s, y, \psi}^{M'_z}$. If the tyre's frequency-response characteristics are determined experimentally using yaw oscillation testing, we can determine $\mathbf{G}_\alpha^{F_y}$ using (3.173) and (3.178):

$$\mathbf{G}_\alpha^{F_y} = \frac{C_\psi^{F_y} - \mathbf{G}_\psi^{F_y}}{p(\sigma + a)}. \quad (3.180)$$

The transfer functions $\mathbf{G}_{\varphi_s}^{F_y}$ and $\mathbf{G}_y^{F_y}$ come from (3.171):

$$\mathbf{G}_{\varphi_s}^{F_y} = \frac{\mathbf{G}_\alpha^{F_y} - \mathbf{G}_\psi^{F_y}}{p} \quad (3.181)$$

and

$$\mathbf{G}_y^{F_y} = -p\mathbf{G}_\alpha^{F_y}. \quad (3.182)$$

Parallel arguments hold for the moment quantities $\mathbf{G}_\alpha^{M'_z}$, $\mathbf{G}_{\varphi_s}^{M'_z}$, $\mathbf{G}_\psi^{M'_z}$, and $\mathbf{G}_y^{M'_z}$. In experiments the whole moment $M_z = M'_z + M_z^r$ is measured and so the M_z^r component must be subtracted before applying the formulas [8]. Another issue relates to the fact that these relationships only hold good within the context of the string model itself, and are only approximations of the physical reality.

3.8 Unsteady magic formulae

The string model analysis demonstrates that there is a lag, related to the relaxation length, in the force and moment responses to slip changes. The idea now is to extend the (steady-state) magic formula to unsteady conditions by using 'relaxed' slips as inputs to the magic formula. Under steady-state conditions this extended model reduces to the original magic formula model. If we restrict our modelling to low frequencies (up to

15 Hz) and large wavelengths ($>1.5 \text{ m} \approx 24a$), which are the conditions usually found when simulating the handling of vehicles, the belt dynamics can be neglected and the force lag can be described using first-order equations [8, 105]. These equations are similar to those derived for the string model in (3.160), (3.161), and (3.162), or (3.164), (3.165), and (3.166), but in this case the relaxation-related quantities are determined experimentally. In general, the relaxation length(s) increase with increased normal load [141], reduce with increasing slip angle [142], reduce with increasing inflation pressure [112], and may increase at high speeds, because of the gyroscopic moments arising from the combination of the belt lateral distortion velocity and tyre rolling velocity [143].

Using the string model as a guide to their general form, the slip relaxation equations we will use are

$$\frac{\sigma_\kappa}{V_{Cx}} \frac{d\hat{\kappa}}{dt} + \hat{\kappa} = \kappa \quad (3.183)$$

$$\frac{\sigma_\alpha}{V_{Cx}} \frac{d\hat{\alpha}}{dt} + \hat{\alpha} = \alpha \quad (3.184)$$

$$\frac{\sigma_{\varphi_s}}{V_{Cx}} \frac{d\hat{\varphi}_s}{dt} + \hat{\varphi}_s = \varphi_s \quad (3.185)$$

in which σ_κ , σ_α , and σ_{φ_s} are the three relaxation lengths in the model and $\hat{\kappa}$, $\hat{\alpha}$, and $\hat{\varphi}_s$ are the relaxed slips (or instantaneous slips), which are filtered versions of the slips κ , α , and φ_s . These relaxed slips are used as inputs for the (nonlinear) magic formulas of Section 3.5 to compute the tyre forces and moments

$$(F_x, F_y, M_x, M_y, M_z) = f(\hat{\kappa}, \hat{\alpha}, \hat{\varphi}_s, F_z). \quad (3.186)$$

To summarize, the extended magic formula model consists of slip relaxation equations (3.183)–(3.185) and the magic formulae in (3.186). It is usually more convenient to use the magic formula defined in terms of γ , rather than φ_s , in which case the σ_{φ_s} and φ_s in (3.185) are replaced with σ_γ and γ . In vehicle dynamics applications the most important relaxation equation is (3.184), which is related to the lateral slip.

The relaxed model has a mechanical analogy that is described using Figure 3.21. A road-contact point \hat{S} is introduced, which is distinct from the wheel slip point S defined in Section 3.2. It is sometimes assumed that points S and C are coincident, which corresponds to replacing the effective rolling radius r_e with the loaded radius r . The velocity difference between S and \hat{S} causes the carcass springs to deflect. The two points are connected by a longitudinal spring $K_x^{F_x}$ and a lateral spring $K_y^{F_y}$, the carcass deformation being \hat{x} in the longitudinal direction and \hat{y} in the lateral direction. The tyre forces are applied to \hat{S} , and depend on the slips $\hat{\kappa}$, $\hat{\alpha}$ and the spin slip φ_s . The longitudinal and lateral slips associated with \hat{S} are computed from their definitions in (3.4) and (3.7)

$$\hat{\kappa} = \kappa - \frac{\dot{\hat{x}}}{V_{Cx}} \quad (3.187)$$

$$\hat{\alpha} = \alpha - \frac{\dot{\hat{y}}}{V_{Cx}}, \quad (3.188)$$

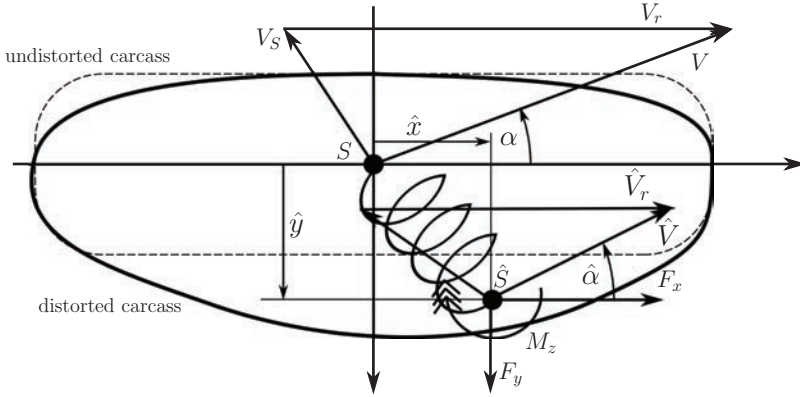


Figure 3.21: Plan view of a single-point tyre model showing longitudinal and lateral carcass deflections \hat{x} and \hat{y} , respectively, which are modelled as linear springs.

where κ and α are the slips associated with S . At \hat{S} there is balance between the forces arising from the spring and the forces arising from the slips

$$K_x^{F_x} \hat{x} = C_\kappa^{F_x} \kappa \quad (3.189)$$

$$K_y^{F_y} \hat{y} = C_\alpha^{F_y} \hat{\alpha} + C_{\varphi_s}^{F_y} \varphi_s, \quad (3.190)$$

where it is noted that the spin-slip thrust $C_{\varphi_s}^{F_y} \varphi_s$ is assumed to develop instantaneously. However, as we will now show, the overall response of the tyre to variation in spin slip is not instantaneous, because of the coupling with the side-slip dynamics in (3.190). When introducing the expressions for slips given by (3.187) and (3.188) into (3.189) and (3.190)

$$K_x^{F_x} \hat{x} = C_\kappa^{F_x} \left(\kappa - \frac{\dot{\hat{x}}}{V_{Cx}} \right) \quad (3.191)$$

$$K_y^{F_y} \hat{y} = C_\alpha^{F_y} \left(\alpha - \frac{\dot{\hat{y}}}{V_{Cx}} \right) + C_{\varphi_s}^{F_y} \varphi_s, \quad (3.192)$$

where the lateral deformation will depend both on the contribution related to forces arising from α and forces arising from φ_s : $\hat{y} = \hat{y}_\alpha + \hat{y}_{\varphi_s}$. The side-slip and spin-slip contributions in (3.192) can now be separated by superposition so that

$$\frac{1}{V_{Cx}} \frac{C_\kappa^{F_x}}{K_x^{F_x}} \left(\frac{K_x^{F_x}}{C_\kappa^{F_x}} \dot{\hat{x}} \right) + \left(\frac{K_x^{F_x}}{C_\kappa^{F_x}} \hat{x} \right) = \kappa \quad (3.193)$$

$$\frac{1}{V_{Cx}} \frac{C_\alpha^{F_y}}{K_y^{F_y}} \left(\frac{K_y^{F_y}}{C_\alpha^{F_y}} \dot{\hat{y}}_\alpha \right) + \left(\frac{K_y^{F_y}}{C_\alpha^{F_y}} \hat{y}_\alpha \right) = \alpha \quad (3.194)$$

$$\frac{1}{V_{Cx}} \frac{C_{\varphi_s}^{F_y}}{K_y^{F_y}} \left(\frac{K_y^{F_y}}{C_{\varphi_s}^{F_y}} \dot{\hat{y}}_{\varphi_s} \right) + \left(\frac{K_y^{F_y}}{C_{\varphi_s}^{F_y}} \hat{y}_{\varphi_s} \right) = \varphi_s. \quad (3.195)$$

The conditions for equivalence between (3.193)–(3.195) and (3.183)–(3.185) are

$$\sigma_\kappa = \left(\frac{C_\kappa^{F_x}}{K_{\hat{x}}^{F_x}} \right) \quad (3.196)$$

$$\sigma_\alpha = \left(\frac{C_\alpha^{F_y}}{K_{\hat{y}}^{F_y}} \right) \quad (3.197)$$

$$\sigma_{\varphi_s} = \sigma_\alpha. \quad (3.198)$$

When side slip and spin slip occur simultaneously, the side slip should be computed using $\hat{\alpha} = \alpha - \hat{y}_\alpha/V_{Cx}$ rather than $\hat{\alpha} = \alpha - \hat{y}/V_{Cx}$ as in (3.188). The relaxation lengths given in (3.196)–(3.198) are the ratios of the tyre slip stiffnesses to the tyre structural stiffness. In this model the relaxation length related to spin slip (or camber) is clearly the same as the relaxation length related to lateral slip. In sum, equations (3.189) and (3.190) are employed when using the mechanical model, and the slips are computed as in (3.187) and (3.188).

In order for the transient model to automatically accommodate relaxation lengths that reduce with reduced normal loads or increasing slips, it is necessary to use the formulation based on the mechanical model in Figure 3.21, instead of that based on the relaxation equations (3.183)–(3.185). The two are equivalent for small slips when the springs are chosen such that (3.196)–(3.198) are satisfied, but for larger slips, the mechanical model has relaxation lengths that automatically reduce, because the numerators in (3.196)–(3.198) reduce, as the slips increase and/or the normal load reduces.

It has been noted experimentally that the lateral force related to camber is composed by a lagged (or relaxed) component (with $\sigma_{\varphi_s} \sim \sigma_\alpha$) and a non-lagged component [97, 142]. This feature can be introduced into the model by replacing φ_s in (3.195) or (3.185) with $(1 - \epsilon_{NL})\varphi_s$, with ϵ_{NL} representing the non-lagged part of φ_s . The input of the magic formula in (3.186) is the sum of the lagged and unlagged components of spin slip. The lagged component is applied on the contact point \hat{S} (as with the other forces), while the non-lagged component is applied directly to the wheel rim at S . The effect of ϵ_{NL} can be considered a secondary effect, which can be neglected in many vehicle dynamics simulations.

When a high-frequency tyre model is required (< 60 – 100 Hz), for ride comfort and vibration analysis for example, the dynamics of the carcass must be included in the model. In this case a rigid ring representation of the belt is usually employed; a flexible belt is necessary when even higher-frequency behaviours are required. The ring is suspended from the rim by (typically six) springs and dampers that represent the carcass compliance. The springs and dampers are then tuned to the frequencies and damping ratios of the lowest natural structural modes of the tyre. Other enhancements may include additional differential equations to model short-wavelength effects, such as overshoots [144], that clearly cannot be treated with a single first-order equation.

The MF-Swift [8, 145] is an example of a model implementing these advanced features.

3.8.1 Low-speed modelling

There are a number of precautions required if tyre models are to behave reliably at very low speeds. For example, V_{Cx} must be replaced by its modulus $|V_{Cx}|$ to allow for backwards running; the slip quantities (κ , α and φ_s) must be protected against zero-speed singularities (usually by adding a small ϵ term to the denominators of these expressions); all of the slip quantities must be limited to $|\kappa| < \kappa^{max}$, $|\alpha| < \alpha^{max}$, and $|\varphi_s| < \varphi_s^{max}$ to avoid unrealistic slip values at low speeds. At speeds below some minimum V^{low} , it may be necessary to enforce $\dot{\kappa} = 0$, $\dot{\alpha} = 0$, and $\dot{\varphi}_s = 0$ when the corresponding slip exceeds some maximum, which may be the slip corresponding to the peak of the associated tyre characteristic.

It can be seen from (3.191) that $\hat{x} \rightarrow 0$ as $V_{Cx} \rightarrow 0$ since \hat{x} must remain bounded. In other words, at very low speeds, the tyre behaves like a spring according to (3.189) and (3.190), and the carcass deflections are given by $\hat{x} = \sigma_\kappa \hat{\kappa}$, $\hat{y} = \sigma_\alpha \hat{\alpha}$ and $\hat{y}_{\varphi_s} = \sigma_\alpha \hat{\varphi}_s$. This low-speed pure-spring property means that the model equations are undamped (eigenvalue on the imaginary axis), and oscillatory behaviours will arise. Therefore, below some low-speed threshold, it may be necessary to add artificially a damper in parallel with the spring (when using the mechanical tyre model), or add a term proportional to V_{Sx} to the relaxed slips $\hat{\kappa}$, $\hat{\alpha}$, and $\hat{\varphi}_s$ (when the relaxation equations are used).

Most of the difficulties associated with low-speed tyre modelling are associated with the forces and moments associated with spin slip. The spring-like behaviour of the tyre at standstill means that the associated models generate an instantaneous spin-slip-related lateral force, whereas the lateral force should be zero (see Section 3.4.3). For this reason the lateral force should be artificially suppressed below a certain low speed V^{low} . It is known that special-purpose models are required for the accurate representation of the moment generated from spin slip at standstill [146].

3.9 Advanced models

There are several models available that are suitable for the simulation of tyre dynamics in a vehicle dynamics context. These models are generally coupled to multi-body software (MBS), which is used to simulate the dynamics of a car, truck, motorcycle, or aircraft.

Among the models with real-time capability, we mention: MF-Tyre, TMeasy, Tame-Tire, MuRiTyre, TRT/GreTa, and MF-Swift. Among the more complex models, which are still suitable for coupling with MBS but much slower than those already mentioned, are FTire and RMOD-K.

MF-Tyre is the official implementation of the magic formulae described above, which are combined with the relaxation equations. At the time of writing the current version is v6.2; however, older versions such as v5.2 (which achieved the status of an ‘industry standard’ for modelling passenger-car tyres in the late 1990s) are still widespread. MF-Tyre is generally used for handling studies with frequency up to 8–15 Hz.

TMeasy [147, 148] is a semi-physical model, which requires empirical slip-force curves (as in MF-Tyre), while the relaxation behaviour is derived from a (physical) carcass model, in much the same way as in the mechanical model described in Section

3.8. Coupling is accounted for using the concept of ‘equivalent slip’, which is similar to that given in Section 3.4.4. The identification of parameters requires only static and steady-state tests. The five parameters used to describe the slip vs force curves are identified for the nominal vertical load, and for twice the nominal vertical load in order to describe the digressive behaviour of the force-generating capability of the tyre due to increasing normal load (see comment around (3.95)–(3.96)). The model can deal with uneven roads as long as the contact patch is closed, that is, at long wavelengths.

TameTire [149, 150] (ThermAl and MEchanical TIRe Emulator) was developed by Michelin in order to include the effects of tyre temperature in vehicle handling simulations. In contrast with the previous models, it does not require the slip vs. force curves. These curves come from a physical model, which includes a flexible carcass described by three main stiffnesses (casing torsion, belt stiffness, and tread stiffness, all depending on load, inflation pressure, and tyre temperature). In the contact region the tread is described by brush elements, whose friction coefficient with the road is dependent on tyre pressure, tyre temperature, and sliding velocity. The brush model is important to determine the sliding region (where heat is generated) and the adhesion region (where the heat is transmitted to the track). The model predicts the average temperature, over a period of rotation on the tyre contact patch, in the belt and in the cavity. The inputs required are the ambient temperature, the road temperature, and the (three) initial tyre temperature(s).

MuRiTyre [151] is a physical discretized multi-rib tyre handling model, which can be parameterized without the requirement for traditional rolling-force and moment data. The number of longitudinal ribs can be increased or decreased in accordance with the processing power available, enabling real-time solutions. The force distribution along each rib is modelled, and used along with the deflected position of the rib, to calculate the ribs’ contribution to the aligning, overturning, and rolling moments of the tyre. The tyre model has mechanical and thermal modes to predict tyre performance with variations in load and temperature. It also includes wear and degradation functions to allow the simulation of performance changes over time and use.

TRT/GrETA [152, 153] is a three-dimensional racing tyre model that takes into account the heat sources, flows, and dissipations in the tyre. The cooling influences of the track and the external air, as well as the heat flows inside the tyre, are modelled. The friction energy developed in the contact patch and the strain energy losses are modelled. The model generates the circumferential temperature distributions in the various tyre layers (surface, bulk, inner liner), as well as the internal heat flows.

MF-Swift [104, 145] (Short Wavelength Intermediate Frequency Tyre) is an extension of the MF-Tyre to higher frequencies ($< 60\text{--}100\text{ Hz}$) and shorter wavelengths ($> 0.1\text{--}0.2\text{ m}$). In this frequency range deformations of the tyre belt can be neglected and the tyre belt can be modelled as a rigid ring that is elastically suspended from the wheel rim. When short obstacles and rough roads are encountered, tyre geometry and elastic effects give rise to the nonlinear behaviours in the tyre forces, and to changes in the effective rolling radius. A 3D obstacle-enveloping model is used to calculate effective road inputs that simulate the tyre’s behaviour as it moves over uneven road surfaces with the obstacle-enveloping behaviour of the tyre properly represented. With this approach a single-point-contact model can be used to simulate manoeuvres such

as a tyre passing over a cleat, where there are three distinct areas of contact: in front of the cleat, on the cleat, and behind it.

FTire [154] (Flexible ring Tyre model) is a development of BRIT [155] (Brush and RIng Tyre model) that comprises structural and tread-road contact models. The structural model uses some 80–200 lumped-mass nodes to model the tyre's cord. These nodes are connected to the rim and to each other by several nonlinear inflation pressure-dependent stiffness, damping, and friction elements. The tread model comprises a number of massless friction elements that are placed between neighbouring belt segments to establish the road contact. These elements are sprung and deflect in accordance with the road profile and sliding velocities. The model also includes a thermal model, which is optionally activated and can compute the temperature of individual tread elements. The model can deal with dynamics up to about 150 Hz, while the computation time is 5–20 times real time. The model has an integrator for the calculation of the belt shape, which runs in parallel with the main integrator, but is synchronized to it.

The RMOD-K models are FEM-based tyre models with different levels of complexity [156, 157]. RMOD-K FEM is a complex nonlinear FEM model with different mesh densities in the structure and contact areas. RMOD-K FB (Flexible Belt) includes a flexible ring, which leads to a significant reduction in computational effort. RMOD-RB (Rigid Belt) is another rigid-ring model that uses an analytical description of the adhesion area, suitable for simulations with frequencies up to 100 Hz on smooth roads. It also includes a thermal model. Finally RMOD-K formula is an open, physical, steady-state tyre model.

Examples of tyre dataset can be found in [8] (car, motorcycle, and truck tyres), [98, 111, 112] (motorcycle tyres), [158] (aircraft tyres), and [159] (bicycle tyres).